Nano Today (2014) **9**, 499—524

Available online at www.sciencedirect.com

ScienceDirect

journal homepage: www.elsevier.com/locate/nanotoday

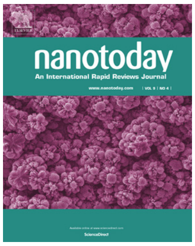

REVIEW

Mesocrystals as electrode materials for lithium-ion batteries

Evan Uchaker[a], Guozhong Cao[a,b,c,*]

[a] *Department of Materials Science & Engineering, University of Washington, Seattle, WA 98195, United States*
[b] *Beijing Institute of Nanoenergy and Nanosystems, Chinese Academy of Sciences, Beijing 100083, China*
[c] *School of Materials Science and Engineering, Dalian University of Technology, Dalian 116023, China*

Received 7 April 2014; received in revised form 31 May 2014; accepted 16 June 2014
Available online 26 July 2014

KEYWORDS
Lithium-ion battery;
Mesocrystal;
Electrode;
Energy storage;
Electrochemistry

Summary Lithium-ion batteries are a well-established technology that has seen gains in performance based on materials chemistry over the past two decades. Although there are many material selections available when assembling such a device, the fundamental design and structure remains the same — two electrodes of different potential separated by an intermediary electrolyte. Despite recent advancements with electrode materials, considerable improvements in energy density and stability are still necessary in order to achieve energy storage parity. The design of structurally oriented nanoparticles can circumvent the thermodynamic instability, undesired side reactions, high processing costs, and potential nano-toxicity effects associated with nanoparticle synthesis, processing, and use. A great deal of recent efforts have focused on the formation and understanding of ordered nanoparticle superstructures with a vast range of architectures; in particular, crystallographically oriented nanoparticle superstructures, or mesocrystals. Mesocrystals can be delineated by their high degree of crystallinity, porosity, and nanoparticle subunit alignment along a crystallographic register. Given their unique combination of nanoparticle properties and order over a microscopic size regime, mesocrystals have strong potential as active materials for lithium-ion battery electrodes. Such assemblies would possess the structural and chemical stability of microsized electrodes while exploiting the beneficial properties associated with nanosized electrodes and their large reactive surface area.

---

* Corresponding author at: Department of Materials Science & Engineering, University of Washington, Seattle, WA 98195, United States. Tel.: +1 206 616 9084; fax: +1 206 543 3100.
E-mail address: gzcao@u.washington.edu (G.Z. Cao).

http://dx.doi.org/10.1016/j.nantod.2014.06.004
1748-0132/

Introduction

Energy use plays an increasingly important role in modern society and has historically been accommodated by considerable daily fossil fuel consumption in order to generate the necessary electricity that powers our modern infrastructure [1]. In turn, the use of and emissions from these combustion sources has led to global concern about energy efficiency, greenhouse gas emission, and resource scarcity. The United States alone spent $502 billion subsidizing fossil fuels in 2011 while an additional $80 billion was spent patrolling oil sea-lanes [2,3]. Moreover, The Energy Information Administration (EIA) projects that world energy consumption will grow by 56% between now and 2040 [4]. Consequently, substantial effort has been made to develop and install renewable energy technologies such as solar panels, wind farms, and hydroelectric instillations. However, the successful implementation of these technologies will be dependent on reliable and robust electrical energy storage given that these energy harvesting methods are intermittent and the majority of energy consumption targets cannot be readily tethered to the grid.

Batteries, as devices for chemically storing energy, possess advantages of high portability, high conversion efficiency, relatively high energy density, long life, and zero exhaust release. They are ideal power sources for portable devices, automobiles, and backup power supplies; accordingly, batteries power nearly all of our portable or mobile electronic devices and are used to improve the efficiency of hybrid electric vehicles as well. Unfortunately, considerable improvements and advancements in rechargeable battery materials and technology are still necessary in order to achieve energy sustainability. More importantly, the energy density, power density, and stability must be vastly enhanced in order to make smart grid and fully electric vehicle technologies an attainable reality. Therefore, developing battery technology, particularly rechargeable batteries, has advanced into a crucial issue for academia and industry over the past several years.

Given all the unique qualities and benefits of nanostructures, the synthesis and characterization of nanostructured electrode materials of various chemistries have been extensively investigated [5—7]. However, the use of nanostructures is not a panacea, and there are several performance issues, either lingering or deriving from nanostructuring, that cannot be overlooked [8]. Conversely, mesocrystals, or mesoscopically structured crystals, are crystallographically oriented nanoparticle superstructures with a typically microsized assembly footprint, and have received much attention since first being introduced [9—11]. The design of microstructurally composed nanoparticle assemblies can, for instance, circumvent the thermodynamic instability, undesired side reactions, high processing costs, and potential nano-toxicity effects associated with nanoparticle synthesis and processing [12—14]. Herein, this review strives to offer a brief outline of the undesired characteristics and limitations associated with nanosized electrode materials, provide a succinct discussion of mesocrystal formation pathways, and then summarize the findings of studies employing mesocrystalline active material electrodes for electrochemical energy storage systems; ultimately, the relationship between the structural characteristics of mesocrystals and their corresponding electrochemical properties is highlighted.

Nanostructured Li-ion battery electrodes

Advantages

Although an overall mature technology, battery design and performance have changed drastically over the past decade with the incorporation and prevalence of nanomaterials [12,15—17]. Size confinement unto the nanoscale leads to enhancement of battery lithiation dynamics by increasing the specific surface area for interfacial Faradic reactions, improving the mass and charge diffusion paths, and modifying the surface thermodynamics (compared to bulk counterparts) which can facilitate phase transitions and eliminate miscibility gaps [18]. Nevertheless, the most dominant and substantial advantages imparted by nanostructuring is drawn from enhancements in the kinetics and corresponding diffusivities because the characteristic time for diffusion is proportional to the square of the diffusion path length [19]. Similar to the effects of transport on Li^+, electron transport is also enhanced in nanometer sized electro-active particles [17].

Studies have also concluded that the implementation of nanostructured electrode materials can lead to specific capacity values beyond the theoretical limits. Such performance effects have been connected with the initiation of new lithium storage mechanisms, usually either *via* a pseudocapacitive storage mechanism that accommodates lithium ions on the surface/interface of the particles below a critical particle size or through a conversion mechanism that involves the formation and decomposition of at least two separate phases through conversion reactions [20—23]. Surface and grain interface effects are more prominent in nanomaterials because of their confined dimensions, making this pseudocapacitive phenomenon even more pronounced. Reversible conversion reactions can transpire between binary MX compounds, where $X = N$, S, F and M is often a transition metal oxide, and metallic lithium and are based on the reduction and oxidation of metal nanoparticles [24—26]; worded differently, it is a reaction that involves heterogeneous lithium storage [27,28]. It has been determined that the reversibility of the conversion reaction depends on complete reduction of the metal species [29]; nanoparticles are extremely effective toward this means because of their large specific surface area that is very active toward the decomposition of the lithium binary compound. Reduction of some micrometer sized materials to the nanoscale has been shown to activate or enable reversible electrode reactions that would otherwise not take place, typically materials with low Li^+ diffusion coefficients. Lithiation in microsized rutile TiO_2 is limited to a negligible amount because of anisotropic Li^+ diffusion that perturbs the rutile framework which successfully blocks Li^+ from occupying thermodynamically preferential octahedral sites [30,31]. There are no such effects in nanoparticle rutile TiO_2 because of the short diffusion length, and significantly more Li^+ can be reversibly incorporated [32].

Similar effects have been observed in nanosized β-MnO_2 [33].

Other studies also revealed that the Li-ion and electron potentials can be modified through the use of exceedingly small particles, producing a change in the electrode potential and overall reaction thermodynamics [16]. Additionally, nanosized electro-active materials can better accommodate the strain associated with Li-ion insertion and extraction, thereby improving the cycle life because they can more readily handle volume expansion and contraction upon de/lithiation, as exemplified by Si nanowires [34]. All of these factors make it possible for nanostructured battery electrodes to more readily approach a higher specific capacity and operate at faster rates [16,35].

Despite years of intensive research accompanied with significant progress, the cathode remains the limiting factor for improved battery performance. Anode materials, even the current commercially available ones, possess stable capacities that are approximately a factor of two better than their cathodic counterparts. Cathode materials on the other hand, are inherently restricted to a considerably lower intercalation capacity and exasperated degradation over long term cycles, at least when compared to their anodic counterparts. Because cathode performance has become a bottleneck for the capacity improvement of lithium ion batteries, research concerning electrodes is more focused on such. In addition to exploring new cathode materials there has also been strong efforts to improve the intercalation capacity of already well-established cathode materials. Several of the material systems that have piqued researcher interest over the years include layered sulfides (Li_xTiS_2), layered transition metal oxides ($LiCoO_2$ and V_2O_5), spinel ($LiMn_2O_4$), and olivine ($LiFePO_4$) structures.

Layered intercalation compounds are one of the more popular material candidates amongst metal oxide electrodes. These layered compounds, for which nearly all of the research and commercialization of cathode materials has been focused, can be further designated into two classes. The first class is comprised of the layered compounds with an anion close-packed or nearly close-packed lattice where the electro-active transition metal ions occupy alternating layers, and lithium is inserted in the unoccupied layers. Both $LiTiS_2$ and $LiCoO_2$, the current commercial cathode of choice, are prime examples of this class of compound. The spinel structured compounds may be classified as a subgroup within this class because the transition metal ions occupy all the layers. Nanostructured $Li_{4+x}Ti_5O_{12}$ spinel has demonstrated superior electrochemical performance when compared to its bulk counterpart due to increased Li-ion occupancy [36]. These results serve as a direct reflection of the enhanced kinetics and transport properties of nanostructured electrodes because the $Li_{4+x}Ti_5O_{12}$ spinel is a zero-strain material. The second class of layered metal oxide compounds can be classified by their more open structures. Primary examples of these structures are the layered vanadium oxides and the tunneled manganese dioxide; the transition-metal phosphates, such as olivine $LiFePO_4$, can also be grouped under this structural classification. The benefits of nanostructuring have been documented for these layered materials as well. Uniform films of V_2O_5 were formed on FTO substrates through a combination of cathodic deposition and catalyzed gelation. The homogenous films were composed of microflakes that ranged from 0.5 to 1.5 μm in diameter, and each flake was composed of nanoparticles measuring 20—30 nm in diameter with 10 nm gaps separating adjacent nanoparticles [37]. Conversely, similar processing routes with the addition of a block copolymer surfactant yielded a porous V_2O_5 structure composed of nanoparticles and pores approximately 100 nm in size [38]. Not surprisingly, the smaller particle and pore size of the surfactant-free specimen led to far greater lithium intercalation capacity (405 *vs.* 275 mA h g^{-1}), rate performance (70 C *vs.* 60 C), and cyclic stability (200 *vs.* 40 cycles). Thinner films displayed similar benefits when compared to thicker films composed of the same electro-active material.

While Li^+ surface storage and increased fracture resistance are performance benefits inherent to many nanostructured electrode materials, an even more complex interaction has been observed in nano-sized $LiFePO_4$ because of its incomplete miscibility gap (region in a phase diagram in which two phases with nearly the same structure have no solubility in one another). Meethong et al. showed that the miscibility gap in pristine $LiFePO_4$ diminishes with decreasing nanoparticle size, suggesting that the miscibility gap completely disappears below some critical value [39]. The enhanced solubility of Li in nano-sized $LiFePO_4$ can be ascribed to the presence of multiple phases in the individual particles. The coexistence of two crystallographic phases within one particle leads to a domain-wall-related energy penalty, which is determined by the strain prompted from the difference in the lattice parameters and can destabilize the two-phase coexistence in smaller particles. Nanostructures have been utilized to increase the equilibrium compositions and effectively reduce the lattice mismatch between coexisting phases. Therefore, the energy gain associated with phase separation will drop with decreasing particle size, and the miscibility gap will gradually diminish [40]. The miscibility gap began to decrease while the solubility increased starting with nanoparticles approximately 100 nm in diameter, and showed a strong effect in particles smaller than 35 nm [41]. Changes in the miscibility gap were ascribed to particle size associated modifications in the molar free energy of mixing for either one or both phases. The associated particle size effects were also speculated to emerge from the relative contributions of the particle-matrix surface energy and stress, and/or the coherency or compatibility stresses in the coherently interfaced two-phase particles [39].

Limitations

One of the most prominent features of nanomaterials is their large specific surface area that has a correspondingly higher surface energy than bulk contemporaries. This large surface energy needs to be factored into the chemical potential of nanoscale materials, and can be approximated by

$$\mu^o(r) = \mu^o(r = \infty) + 2\left(\frac{\gamma}{r}\right)V, \qquad (1)$$

where γ is the surface tension, r the particle radius, and V the partial molar volume [20]. As previously mentioned, this large and energetically relevant surface area can contribute to a pseudocapacitive Li^+ storage mechanism [42—45]. However, there are several shortcomings and limitations that can be categorized as direct consequences of this additional free surface energy.

Diminished voltage plateaus and curved voltage profiles have both been attributed to the strain and interfacial energy from coexisting lattice terminations within electrode nanoparticles. These differing structural environments in the near-surface region result in a distribution of the redox potentials; varying structural environments depend on the distance from the surface and the surface orientation itself, verifying that size and morphology play an important role in dictating particle stability [46]. Hence, the irreversible capacity can be larger for smaller particles with a surface area greater than some critical value, where the optimal particle size is dictated by the voltage window [47]. Moreover, too high of Li-ion intercalation at the surface leads to passivation of the surface region by surface reconstruction or mechanical failure, and accompanying irreversible capacity loss is inevitable [48,49]. Thus, there exists an optimal particle range for nanomaterials where cracks resulting from non-surface related volume expansion will not propagate, and surface reconstruction will not occur [50].

Expanding upon this, the formation of the solid electrolyte interphase (SEI) is even less predictable in nanomaterials because of their high surface area and corresponding high surface energy that increases the potential for secondary or side reactions along the specific surface area of the particle. The SEI layer is a film that forms on the surface of the electrode through the decomposition of the electrolyte into lithium containing organics and inorganics in an attempt to reduce the contact area and thereby prevent further electrolyte decomposition [51]. The formation of a stable SEI is often critical because it can act as an interfacial stabilizer and improve the capacity retention of the electrode over long cycle lifetimes at the expense of a large irreversible capacity drop because its ionic and electronic conductivities are relatively low and it effectively intercepts and stores Li^+ that would otherwise be intercalated by the electrode [52]. However, a non-uniform, thick, and unstable SEI can have unfavorable impact on electrode performance, and is more likely to be present in nanomaterials rather than their bulk counterparts. Past studies have clearly demonstrated the deleterious effects of SEI formation on nanostructured electrodes. It was confirmed that a thicker SEI would form on $LiCoO_2$ as the particle size decreased [53]. The thicker layers negated the positive effects of nanostructuring the electrode material by severely impeding Li-ion diffusion, and diminishing the electrode performance at higher current densities. Similar results were seen for $LiMn_2O_4$ where the SEI thickness on a cycled electrode increased in a near linear fashion with the number of cycles, and the cycle stability was the performance parameter most impacted [54].

Another issue concerning the size-stability of nanoparticles is the propensity of the electro-active metal ion to dissolve in the electrolyte, resulting in cyclical capacity degradation [55]. The majority of cases documenting the dissolution of the electro-active metal ion have focused on $LiMn_2O_4$, where Mn-ions in the electrode are easily dissolved into the electrolyte by acids generated *via* oxidation of the solvent molecules, but the process can occur in any Li_xMO_y phase [56—58]. Migration of the dissolved species to the anode can have fatal effects on the functionality of the cell; their precipitation on the anode terminal destroys the passivation layer on the negative electrode and can lead to plating [59]. However, dissolution can be prevented by applying an oxide coating on the nanoparticles to decrease the surface area and eliminate any side reactions [60]. The stabilized electrochemical operating voltage range for nanostructured electrode materials also becomes narrower, compared to bulk materials, during electro-active material dissolution.

Electronic and ionic conductivity have long been limiting factors to the development of electrode materials for Li-ion battery [61]. These barriers stem from several fundamental issues: (i) the metal oxide materials typically employed as cathodes have relatively low electronic conductivity, (ii) a complex relationship between the electrical and ionic conductivities in electrodes, and (iii) phase transformations upon lithiation that can change the conductive properties. Additionally, it has been well established that nanomaterials suffer from resistivity much greater than their corresponding bulk material; nanowires, for example, typically display resistivity values that are ~20% greater than what is seen in the bulk regime, and this discrepancy can extend up to several orders of magnitude [62]. The reason for the drastic increase in the resistivity of nanomaterials is due to the surface scattering of electrons as a result of the sheer increase in the relative surface area and the number of grain boundaries that is strongly dependent on the particle size and morphology [63]. These physical parameters negatively impact the conduction mechanisms because of the inelastic scattering of conduction electrons at particle surfaces and the reflection of electrons at grain boundaries. These effects are also more pronounced in the electrode materials with smaller mean particle size. To compensate for these effects, conductive additives such as carbon are typically added to electrodes, but such inclusions decrease the already low packing density of nanostructured electrode materials even further.

Tortuosity is one of the most important parameters to characterize a porous medium, and reflects the reduction in transport within the electrode due to the complex porous structure comprised of active particles, binder, and conductive carbon [64—66]. Complex, tortuous nanostructures can lead to decreased effective electrolyte conductivity and diffusivity for porous electrodes by limiting transport in the electrolyte phase. The concept of electrode tortuosity (τ) is used along with electrode porosity (ε) as a measure for the decrease in effective electrolyte conductivity and diffusivity due to the structure of the electrode within the confines of the porous electrode description; the tortuosity of a material should decrease as the porosity increases, and Bruggeman suggested a quantitative relationship between porosity and tortuosity that is often used in battery models [67,68]

$$\tau = \varepsilon^{-\alpha}, \tag{2}$$

where α is defined as the Bruggeman exponent which is typically taken to be 0.5 as an appropriate value to describe the pore volume of a packing of equally sized spheres [69]. The minimization of induced polarization losses associated with interfacial, concentration and ohmic loss processes have led to improvements in battery energy and power density [70]. Tortuous transport paths result in a higher macroscopic ohmic resistance, which in turn hinders the delivered energy and power density. Based on geometrical constraints, nanoparticle based electrodes would have less effective packing with a large amount of small pores that would ultimately hinder electrolyte penetration and thus negatively affect the tortuosity, conductivity, and diffusivity.

Processing conditions are also heavily impacted by the high reactivity of nanoparticles. Many nanomaterials exhibit poor stability when exposed to ambient atmosphere; such is the case for olivine $LiFePO_4$ due to the high reactivity of Fe^{2+} in the presence of atmospheric oxygen and water. This undesired reaction under ambient exposure is known to be more pronounced for smaller particles because of their increased surface/exposure area, and can result in spontaneous lithium extraction and surface oxidation [71]. It has also been revealed that nanostructured electrode materials with poor adherence to the current collector will agglomerate during cycling; nano-SnSb undergoes successive agglomeration during Li^+ insertion and extraction, and experiences quick capacity fade as a result [72]. Inactive $LiMO_y$ phases with the transition metal cations of lower oxidation are formed from redox reactions with solution species [59]; moreover, these compounds can be spontaneously delithiated under ambient conditions involving reactions with CO_2 [73]. Thus, the application of some electro-active materials may be limited due to the high processing costs associated with avoiding these secondary reactions and stability issues.

An additional limitation stemming from the use of nanomaterials relates to their packing density or mass loading, which is the amount of active material per unit area of an electrode. There are several characteristics that must be strictly controlled in order to assure a homogeneous and ideal electrode mass loading; such features include the physical composition, packing density to maximize active material content, and open porosity to access the electrolyte. Ultimately, the desired mass loading is dictated by and should reflect the diffusion coefficient of lithium ions, electrical conductivity of particles, and electronic continuity to guarantee charge exchange to the current collectors. The standard thickness and mass loading for a typical commercial electrode is $50\,\mu m$ and $20\,mg\,cm^{-2}$, respectively [74]. However, the overwhelming majority of commercially available cells employ microsized electrodes because the mass loading of nanosized particles is far less than this value, typically $1-2\,mg\,cm^{-2}$ [75,76]. Given that the density of a nanomaterial is generally less than the same material formed from micrometer-sized particles, the volumetric energy density is effectively limited in nanomaterial because there is a larger ratio of components not participating in the electrochemical reaction (such as binding agent or conductive additives) [12,17]. In fact, carbon black additives can constitute 80—98% of the composite electrode surface area as governed by the average particle size [77].

Mesocrystal formation pathways

Provided the shortcomings of nanostructured electrode materials, it should come as no surprise that researchers have been working to exploit the preferential characteristics of nanomaterials while attenuating their deficiencies and limitations — namely by combining nano and macro effects [78—80]. The International Union of Pure and Applied Chemistry (IUPAC) has designated three separate categories in which porous solids can be categorized, depending on pore diameter: microporous ($d < 2$ nm), mesoporous ($2\,nm < d < 50\,nm$), and macroporous ($d > 50$ nm). Examples of microporous materials include zeolites and their derivatives, while xerogels and aerogels are commonly examples of mesoporous materials [63]. Mesocrystals cannot be confined to one pore size regime because the pore size and distribution is specific to each case; a brief overview of their synthesis techniques and formation pathways will be provided in this section.

There has been considerable efforts carried out in the synthesis and characterization of ordered nanoparticle superstructures with a vast range of architectures, also known as mesocrystals. As initially described by Cölfen and Antonietti, mesocrystals, short for mesoscopically structured crystals, are crystallographically oriented nanoparticle superstructures [9—11]. For some time, mesocrystals were only studied in biomineral materials, but current research efforts have shifted to the development of mesocrystalline organic molecules, metal oxides, and other functional materials [81].

To date, novel nanoparticle arrangement has been achieved with colloidal crystals and supercrystals or nanocrystal superlattices; however, individual nanoparticle orientation is not taken into account under these systems. Similar to these systems, mesocrystals can be classified by their high degree of crystallinity and high porosity, but differentiate themselves with subunit (individual nanoparticle) alignment along a crystallographic register. These highly desirable properties are due in part to mesocrystal formation mechanisms, which are still poorly understood, and make mesocrystals the ideal material candidates for catalysis, sensing, and energy storage and conversion applications. Porous materials with large specific surface areas have been shown to enhance the performance of lithium ion battery electrode materials because of more prevalent and uniform pores that ease intercalation by decreasing the Li^+ diffusion distance and pathways. Thus, mesocrystalline materials could be exceedingly beneficial when used as electrode for electrochemical energy storage devices, particularly Li-ion batteries, because of the inherent and uniform porosity associated with the well-defined nanoparticle orientation [82].

Mesocrystal growth often proceeds *via* the aggregation of precursor units, more specifically as homoepitaxial aggregation of primary units, rather than by the classical ion-by-ion growth mechanism [83]. This non-classical growth process can be attributed with the generation of crystals with hierarchical structures and complex morphologies [10]. Organic additives are commonly used to facilitate this process, but are not required by any means [84]. The oriented assembly of nanoparticles leads to the formation of mesocrystals where the constituting crystallites are arranged along a shared crystallographic register and the product particles demonstrate single crystal behavior. The fusion of the primary nano-subunits can lead to single-crystalline structures with included organic additives as defects. Mesocrystal intermediates can also fuse to form single crystals with included organic additives, sometimes allowing the

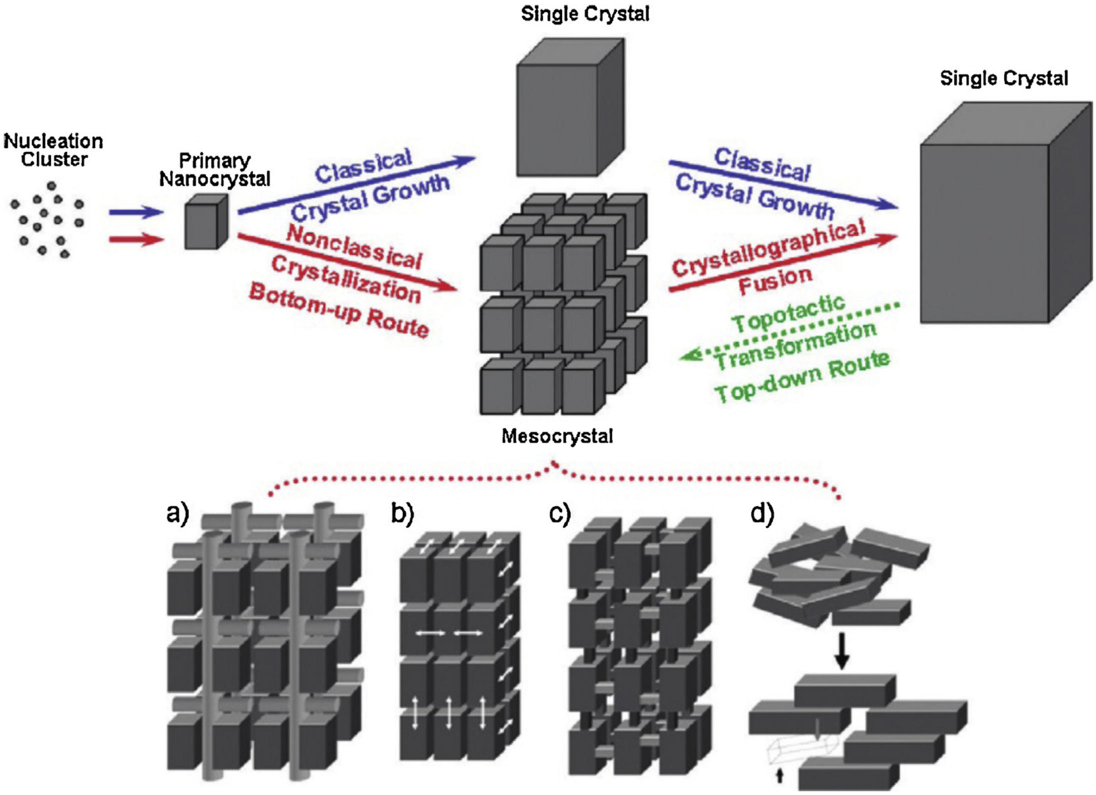

Figure 1 Exemplified mesocrystal formation pathway starting with cluster-seed nucleation and growth of a primary nanoparticle subunit followed by: (blue route) classical crystallization *via* ion-by-ion attachment *versus* (red route) single-crystal formation with a mesocrystal intermediate composed of oriented nanoparticles. (a—d) Schematic of the four principal nanoparticle orientation pathways: (a) ordering by an organic matrix, (b) physical fields or interparticle forces, (c) mineral bridge connections, and (d) spatial constraints.

Reprinted with permission from Zhou et al., J. Phys. Chem. Lett., 2012, 3, 620—628. Copyright 2012 American Chemical Society [80].

observation of highly oriented nanoparticle-based intermediates. Identification of mesocrystals has proven to be difficult but can be achieved *via* the detection of a number of features including high porosity/large surface area, evidence of mesoscopic subunits, and single crystal electron diffraction traits as observed from transmission electron microscopy (TEM) [85].

Studies considering the formation mechanism of mesocrystals have indicated that nanoparticle, colloidal stabilization, and long-range interaction potentials play prominent roles in deciding the formation process. The interaction between individual nanoparticle surfaces plays a critical role during the formation steps, and can lead to the exposure of specific (high energy) facets. It has been demonstrated that the control of particular electrode material crystal facets is beneficial for lithium ion storage as well as catalytic processes [86—89]. These increased attributes can be ascribed to the unique surface properties of specific facets, including the surface energy and diffusion barrier [90,91]. However, a complete picture of the formation mechanism and predictable control of the resulting product has yet to be accomplished, but emphasis has been placed on the different possible forces that may drive orientation and assembly between nanoparticles. It is speculated that the main mesocrystal formation pathways include: ordering by an organic matrix, physical fields or interparticle forces, mineral bridges, space constraints; moreover, there are several other, less likely, formation mechanisms that include topotactic reactions, gel/polymer-mediation, or a combination of these mechanisms [11,84]. A schematic of the four principal formation pathway possibilities are shown in Fig. 1a—d, but it should be noted that many of the pathways are still conjectural.

Interestingly, the formation mechanisms of zeolites are very similar to those of mesocrystals, both in their functionality and lack of comprehensive understanding. R.L. Penn has put forth several nice works that summarize oriented aggregation [92,93]. Due in part to their structure, open-framework materials, such as zeolites, are ideally suited for fast-ion conductor applications because of their open channels that provide pathways for facile ion migration. Unfortunately despite their structural framework of open channels and cages, strong interaction between the oxygen framework and extra-framework charge carriers, such as Li^+ and Na^+, prevent zeolites from being used as fast-ion conductors [94]. For extensive information describing zeolite formation, the reader is referred to several excellent works [95,96].

Table 1 Summary of physical and electrochemical characteristics of mesocrystalline anode materials.

Reference	Material	Phase	Overall morphology	Overall size (nm)	Subunit morphology	Subunit size (nm)	Initial capacity (mA h g^{-1})
[104]	TiO_2	Rutilc	Nanorod bundle	300	Rod	3–5	171 (1 C)
[105]	TiO_2	Rutile	Octahedral	300	Wire	60	154(1 C)
[106]	TiO_2	Anatase	Ellipsoidal	280–380	Particle	20	152 (2 C)
[107]	TiO_2	Rutile	Dumbbell	600–800	Wire	3–5	103 (5 C)
[107]	TiO_2	Anatase	Truncated-octahedra	25–50	Particle	3–5	124 (5 C)
[109]	SnO	Tetragonal	Layered plate-like	800	Sheet	40	535 (0.1 C)
[109]	SnO	Tetragonal	Layered nesl-like	700	Sheet	40	460 (0.1 C)
[109]	SnO	Tetragonal	Layered bipyramid	900	Sheet	40	352 (0.1 C)
[110]	SnO_2	Tetragonal	Nanorod array	80	Rod	10	980 (0.2 C)
[113]	CuO	Tenorite	Nanoleaf	300	Particle	3	674 (1 C)
[114]	Fe_2O_3	Hematite	Spherical	2500	Rod	40	840 (0.2 C)
[115]	Fe_2O_3	Hematite	Rhombic	200	Particle	10	756 (0.1 C)
[115]	Fc_2O_3	Hematite	Ellipsoidal	400	Particle	10	512(0.1 C)

Mesocrystals as Li-ion battery electrodes

Negative electrode materials

There have been considerable research efforts conducted on the synthesis and electrochemical characterization of simple metal oxides, primarily used as anodes for lithium ion batteries. In the following section, we will focus our discussion on mesocrystals of TiO_2, SnO_x, CuO, and Fe_2O_3. The physical and electrochemical characteristics of these systems have been compiled and are shown in Table 1.

TiO_2

The majority of the work on anodic electrode materials has focused on TiO_2 and its derivatives because of its proven safety, good cyclic stability, and high rate performance [97–99]. Initial reports of TiO_2 mesocrystals focused on the topotactic conversion of NH_4TiOF_3 [100,101], and were followed with the synthesis of rutile TiO_2 through the use of organic additives [102,103]. Hong et al. were among the first to develop rutile TiO_2 mesocrystals using an additive free, low temperature synthesis process [104]. TiO_2 nanowires were first synthesized by hydrothermal growth, and were then dispersed in an aqueous acid dispersion to yield mesocrystal bundles through homoepitaxial aggregation. Fig. 2a shows a typical TiO_2 mesocrystal with length and diameter of 300 and 70 nm, respectively, as imaged with TEM. The inset images in Fig. 2a reveal that the mesocrystal is in fact composed of bundled TiO_2 nanorods with diameters of 3–5 nm, while the corresponding selected area electron diffraction (SAED) pattern verifies the single crystal characteristics of the overall bundle. Higher resolution TEM images further confirm the presence of homoepitaxially oriented nanowires as well as their growth along the [0 0 1] direction.

Fig. 2c presents the rate capability of the rutile TiO_2 mesocrystals from 0.5 to 5 C (1 C = 170 mA g^{-1}) for 10 cycles at each incremental current rate. The TiO_2 mesocrystals demonstrated good rate performance and delivered a large stable capacity of 200 mA h g^{-1} at 0.5 C; furthermore, the mesocrystals had a stable reversible capacity of 171.3 mA h g^{-1} after 100 cycles at 1 C (Fig. 2d). The enhanced lithium storage properties were ultimately attributed to the mesoscopic structure of the rutile TiO_2 mesocrystals, which offered a large specific surface area of 38.5 m^2 g^{-1} and short transport distance as evinced by the low volume of mesopores. Both of these factors would facilitate lithium-ion intercalation at the interface, shorten both the mass and charge transport distances, and better accommodate any volume change accompanied with lithium-ion intercalation.

A mechanism for the formation of the rutile TiO_2 mesocrystals in the absence of polymer additives was proposed to occur through the homoepitaxial aggregation of hydrogen titanate single crystal nanowire subunits, as depicted in Fig. 2e. It is proposed that Brownian motion would bring two titanate nanowires in contact and would then be held together by weak the van der Waals forces. The attractive force between two hydrogen titanate nanowires would be rather weak since the Hamaker constant of water is more than an order of magnitude larger than that of hydrogen titanate, giving rise to the formation of mesocrystals. Additionally, the acidic conditions would ensure a relatively slow condensation reaction between the two nanowire surfaces, allocating for better crystal orientation prior to aggregation. It should also be noted that aggregation along the [0 0 1] direction provided the maximum attachment among neighboring nanowires, and the greatest reduction in surface energy. It is also proposed that the slow phase transformation at low temperature accounted for the stability of the mesocrystal against fusing into single crystal. Interestingly, Wulff-shaped octahedral and nanorod-like nanoporous mesocrystals composed of ultrathin rutile TiO_2 nanowires were produced when the surfactant sodium dodecyl benzene sulfonate (SDBS) was introduced into the reaction system [105]. The morphology of the mesocrystals depended largely on the content of the SDBS, specifically

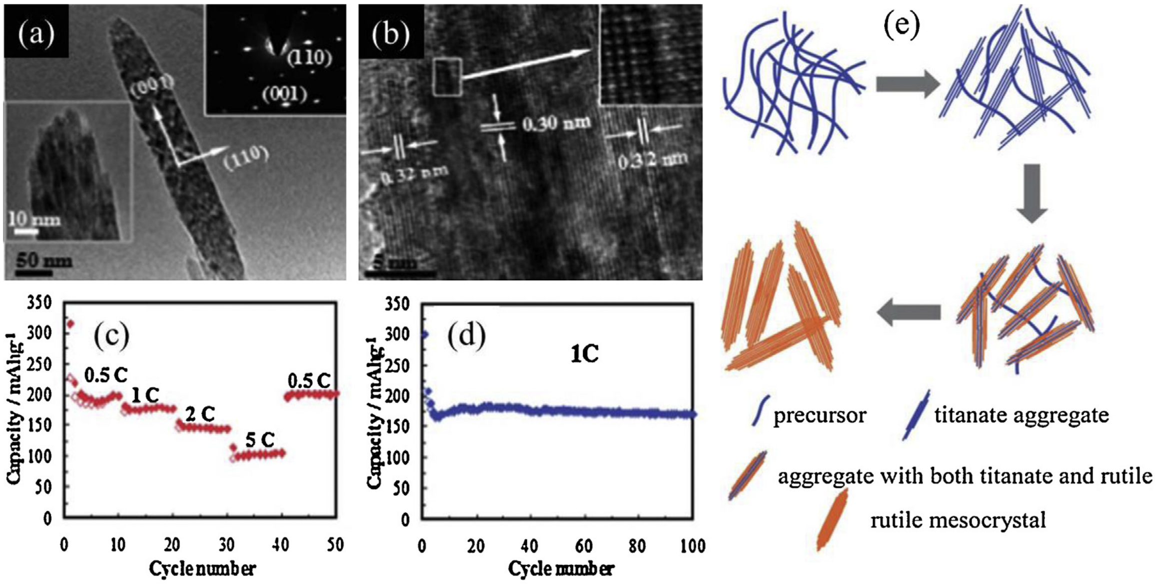

Figure 2 (a) Representative and (b) high-resolution TEM image of rutile TiO_2 nanowire bundled mesocrystals. Upper insets show corresponding SAED patterns. (c) Rate capability from 0.5 to 5 C, (d) cycling performance at a constant current rate of 1 C, and (e) schematic of the proposed formation mechanism for the rutile TiO_2 mesocrystals.
Reproduced from Ref. [104] with permission from The Royal Chemistry Society.

the titanate/SDBS ratio, resulting in rutile mesocrystals with different shapes. Again, the mesocrystals formed through homoepitaxial self-assembly of nanocrystallites, but this time with the assistance of the SDBS additive.

As opposed to rutile TiO_2, Ye et al. synthesized ellipsoidal anatase TiO_2 mesocrystals approximately 380 nm in length and 280 nm in diameter though the solvothermal reaction of acetic acid and tetrabutyl titanite (TBT), the end result of which is shown in Fig. 3 [106]. The mesocrystalline structures displayed a seemingly rough surface and were composed of oriented nanoparticles ranging between 10 and 20 nm in diameter. SAED confirmed the single crystalline characteristics of the mesocrystal and revealed that the elongated ellipsoid direction corresponded to the [0 0 1] direction, as observed in the inset of Fig. 3c. Time dependent growth investigations revealed that the mesocrystals formed through a series of several chemical reactions involving ligand exchange, esterification, hydrolysis-condensation, and finally transient metamorphosis.

It is desirable to develop additive-free solution routes considering that the organic additives usually employed in mesocrystal synthesis are too costly for wide-spread application. Toward this means, the acetic acid solvent played multiple roles during the mesocrystal formation process. The acetic acid acted as a chemical modifier and lowered the reactivity of TBT while reacting with it to form metastable precursors for the slow release of soluble titanium-containing species so that nascent anatase nanocrystals were continuously being formed. Acetic acid reacted with TBT to yield butyl acetate that operated as a templating agent during oriented aggregation and the nanocrystals were stabilized by acetic acid, thus preventing single crystal formation and eventually leading to mesocrystal formation along the [0 0 1] direction through the oriented attachment mechanism.

The mesocrystalline nature of the particles was most likely achieved through the oriented attachment mechanism and infusion between the TiO_2 nanoparticles, leading to a decrease of the interfacial nucleation sites for the rutile phase. The formation of the TiO_2 mesocrystals through the oriented attachment mechanism also decreased the number of grain boundaries existing between individual TiO_2 nanoparticles, thus resulting in facile electronic conduction and fast Li^+ transport between the electrolyte and the mesocrystal electrode. The uniformly dispersed nanopores throughout the structure of the mesocrystals can facilitate their contact with the electrolyte, hence increasing the electrode/electrolyte interface which favors fast Li^+ transport. These speculations were validated when the mesocrystal TiO_2 anode was compared to a TiO_2 anode composed of nanoparticles of approximately the same size as the mesocrystalline subunits, approximately 15 nm (Fig. 3e). The capacity of the mesocrystals and nanocrystals were comparable at lower current densities. However, the mesocrystalline anode considerably outperformed its nanoparticle counterpart at higher current rates, 152 $mA\,h\,g^{-1}$ compared to 115 $mA\,h\,g^{-1}$ at 2 C (1 C = 170 $mA\,g^{-1}$), respectively, while demonstrating an overall good rate capability. The mesocrystals also demonstrated good cycle stability, with approximately 74.2% of the initial 205 $mA\,h\,g^{-1}$ discharge capacity retained after 60 cycles at 1 C.

Expanding upon their previous work, Hong et al. went on to control the morphology of both rutile and anatase TiO_2 mesocrystals through the use of different counterions during synthesis [107]. Dumbbell shaped rutile TiO_2 mesocrystals were obtained when an HCl aqueous solution was used (Fig. 4a and b), while truncated-octahedral anatase TiO_2 mesocrystals were obtained when the aqueous solution was H_2SO_4 based (Fig. 4c and d). The dumbbell shaped rutile TiO_2 superstructures were approximately 600—800 nm in

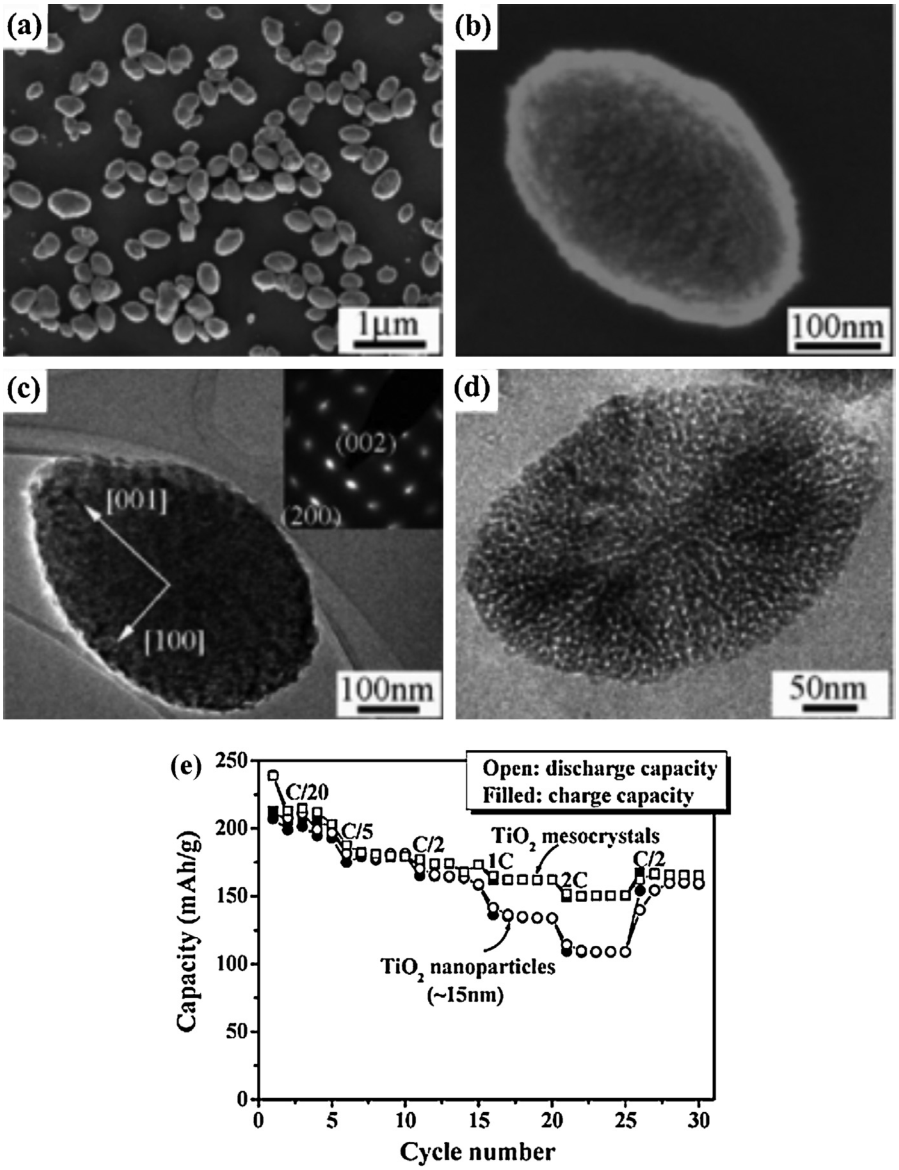

Figure 3 (a and b) SEM images, (c and d) TEM images, and (e) electrochemical performance of nanoporous anatase TiO_2 mesocrystals.
Reprinted with permission from Ye et al., J. Am. Chem. Soc. 2011, 133 (4), 933—940. Copyright 2011 American Chemical Society [106].

length, and assembled from thin nanowires with average diameters of 3—5 nm grown along the [0 0 1] direction. Nitrogen sorption analysis measured the specific surface area at 12.6 $m^2\,g^{-1}$ and revealed that the sample had a low volume of mesopores.

The samples treated with an aqueous H_2SO_4 solution produced truncated-octahedral anatase TiO_2 mesocrystals measuring 25—50 nm that were made up of 3—5 nm sized nanoparticles. SAED was used to determine that the nanoparticle subunits were highly oriented along the [101] direction and elongated along the [0 0 1] direction, seemingly adopting a formation of Wulff-shaped anatase mesocrystals corresponding to the principles of single crystal growth [86,105]. These results indicate that the truncated-octahedral anatase TiO_2 mesocrystals were a single crystal intermediate. The Brunauer—Emmett—Teller (BET) nitrogen sorption derived surface area and total pore volume was 225 $m^2\,g^{-1}$ and 0.43 $cm^3\,g^{-1}$, respectively. The anatase mesocrystals had a narrow micropore size distribution of approximately 0.5 nm, while the average mesopore was approximately 18 nm.

A proposed formation mechanism for the counterion controlled TiO_2 superstructures is depicted in Fig. 4e. It has been well documented that the titanate precursor has a layered structure made up of edge sharing TiO_6 octahedra with H^+ or K^+ occupying the interlayer spaces. The TiO_6 octahedra will rearrange under acidic conditions into either anatase, which is assembled from four edge and corner sharing octahedra, or rutile, which is assembled from two edge and corner sharing octahedra. Based on geometrical considerations, linear chains can only form rutile-type nuclei whereas skewed chains can only form anatase-type nuclei

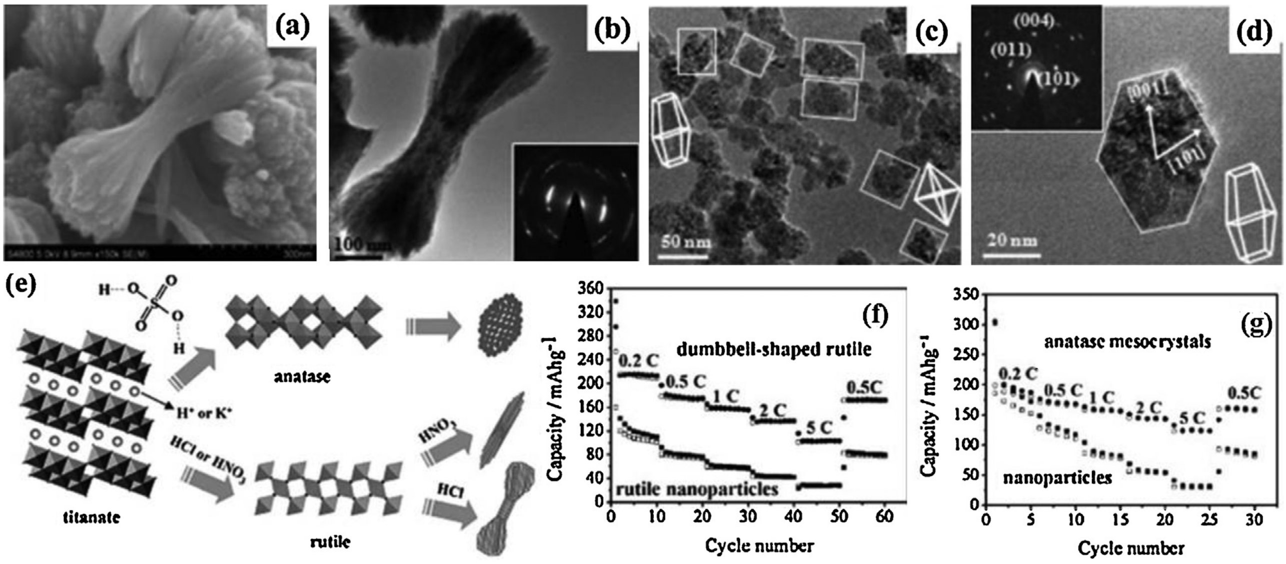

Figure 4 (a) SEM and (b) TEM images of the rutile TiO_2 dumbbell mesocrystals, (c and d) TEM images of the truncated-octahedral anatase TiO_2 mesocrystals, (e) schematic of the proposed formation mechanism of TiO_2 superstructures with different morphology and phase. The insets in (b and d) are the corresponding SAED patterns. Rate capability of the (f) dumbbell shaped rutile, and (g) truncated-octahedral anatase TiO_2 mesocrystals and comparison with similarly sized commercially available particles of the same phase (open-discharge, filled-charge).

Reprinted with permission from Hong et al., Chem. Eur. J. 2012, 18, 10753—10760. Copyright 2012 John Wiley & Sons, Inc. [107].

[108]. Thus, the titanate nanowire precursor kept its morphology when subjected to acidic conditions except when exposed to $[SO_4^-]$ because of its steric hindrance effects. Therefore, the titanate nanowires readily decomposed to nanoparticles in the presence of H_2SO_4; in either case, the mesocrystals formed through oriented aggregation.

The galvanostatic charge-discharge performance as a function of current density for both the rutile and anatase mesocrystals was compared to nanoparticles of their corresponding material and size; both mesocrystal specimens demonstrated their advantages. At a discharge rate of 5 C, the rutile mesocrystals had a discharge capacity of 103 mA h g^{-1}, while the rutile nanoparticles only exhibited 28 mA h g^{-1}. Equivalent differences in specific capacity were observed at lower current densities as well, attesting to the overall superiority of the mesocrystal material as revealed in Fig. 4f. Similarly, the anatase mesocrystals exhibited a discharge capacity of 124 mA h g^{-1}, while the anatase nanoparticles only exhibited 32 mA h g^{-1} at a discharge rate of 5 C (Fig. 4g). For the anatase mesocrystal, discrepancies in the capacity were more pronounced at higher discharge rates and less noticeable at lower current density. The improved Li^+ intercalation rate performance was attributed to the intrinsic characteristics of the mesoscopic TiO_2 superstructures, which had a single crystal-like and porous nature which facilitated fast electron transport and relieved the strain from volumetric change.

SnO_x

In addition to TiO_2, tin oxide is another widely used and investigated inorganic anode material compound because of its ease of fabrication and high theoretical capacity (875 mA h g^{-1} for SnO and 782 mA h g^{-1} for SnO_2). SnO hierarchical nanostructures were synthesized *via* the direct decomposition of tin oxide hydroxide to yield layered plate-like, nest-like, and stepwise bipyramid-like SnO mesocrystals constructed from SnO nanosheets [109]. The morphology of the resulting mesocrystal was controlled by adjusting the $Sn_6O_4(OH)_4$ decomposition reaction rate by regulating the amount of injected water. Plate, nest, and pyramid like superstructures were obtained using incrementally greater amounts of water, respectively. SEM results revealed that the products were all composed of nanosheets oriented with respect to one another in some manner. The plate-like structure was approximately 800 nm in diameter and 300 nm thick, as shown in Fig. 5a, where the nanosheets were stacked orthogonal to the plate surface. The nest-like structure (Fig. 5b) was derived when the amount of water injected during the reaction was increased. The nest-like superstructure was comprised of radially oriented, smaller, nanosheets into an overall size of approximately 700 nm. Further increases in the amount of injected water induced the formation of a stepwise bipyramid-like structure with an average length of 2 μm. The size of the stacked nanosheets constituting the stepwise bipyramid-like structure varied along the longitudinal axis of the pyramid, but fell in between 300 and 900 nm. The nanosheets were approximately 40 nm thick, as determined from SEM image shown in Fig. 5c. The peaks from the corresponding XRD spectra became more intense and narrow when more water was injected during the reaction process, meaning that the crystallinity of the resulting SnO product was enhanced upon the injection of more water. TEM and SAED examination lead to the conclusion that nanosheet aggregation along the [0 0 1] direction *via* the attachment of (1 1 0) facets can significantly decrease the energy of the system by eliminating high energy facets. These results successfully demonstrate that water could be used to efficiently modify the decomposition

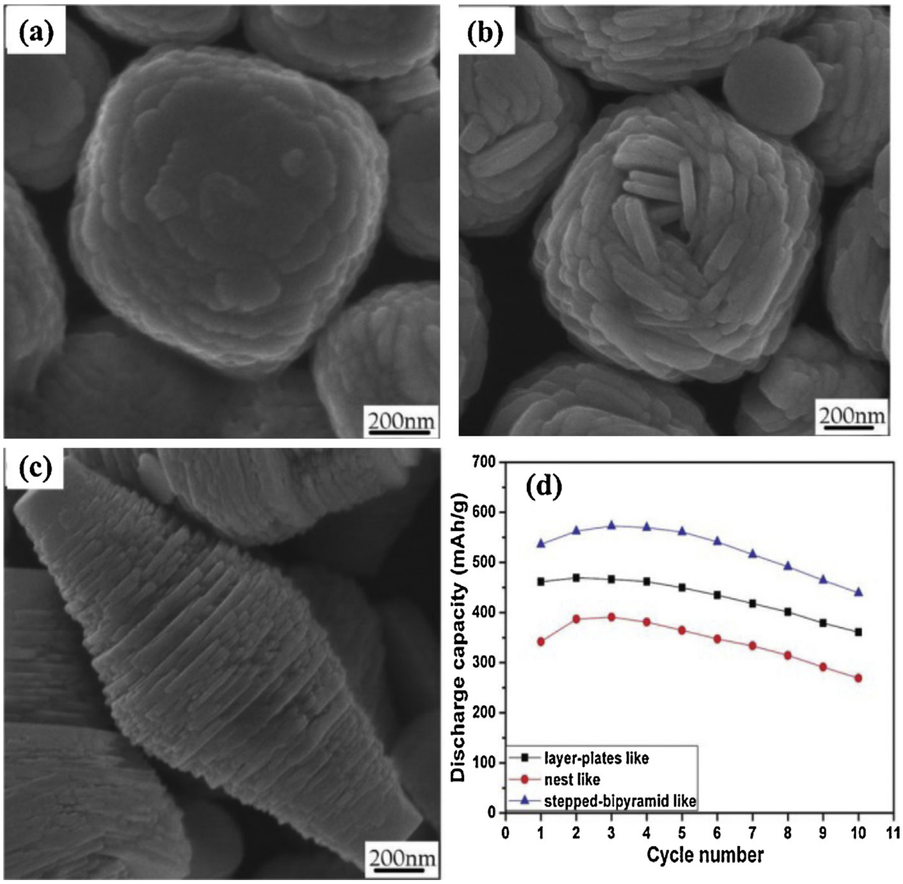

Figure 5 SEM images of (a) layered plate-like, (b) nest-like nanostructures, and (c) stepwise bipyramid-like SnO mesocrystals; (d) cycle stability of the respective electrodes.
Reprinted with permission from Ning et al., J. Phys. Chem. C 2009, 113, 14140—14144. Copyright 2009 American Chemical Society [109].

of $Sn_6O_4(OH)_4$ to SnO by reducing the overall reaction rate of the system through the incorporation of water. Therefore, SnO nanosheets would have more time to grow and aggregate by increasing the amount of injected water, leading to the formation of the various mesocrystals.

As shown in Fig. 5d, the various SnO mesocrystals demonstrated distinct electrochemical characteristics which could be attributed to the different morphologies. The stepwise bipyramid, plate, and nest like structures exhibited initial capacity values of 535, 460, and 352 mA h g^{-1}, respectively, at 100 mA g^{-1}. These results clearly establish that the morphology plays the largest role in modifying the electrochemical performance; no correlation is drawn from crystallinity. Although they were the overall largest structure, the stepwise bipyramid-like mesocrystals may have had the highest overall capacity because they were made up of the smallest nanoparticle subunits. These small nanoparticle subunits resulted in lower diffusion barriers and better accommodation of Li^+ induced strain. The degree of nanoparticle orientation for the bipyramid and plate like structures was better than that of the nest like crystal, and was reflected in the electrochemical performance results. However, all of the SnO structures displayed moderate capacity fading upon cycling, even after just 10 cycles.

Chen et al. reported on a facile kinetics-controlled growth mechanism of aligned arrays of SnO_2 mesocrystalline nanorods in a unique ternary solvent system comprising acetic acid, ethanol, and water [110]. The use of multiple solvents allocated for precise control of solute supersaturation, which was ultimately used to regulate the heterogeneous nucleation and subsequent morphology of the mesocrystalline SnO_2 nanorod arrays. SnO_2 nanorod arrays were solvothermally fabricated on Ti foils using $SnCl_4$ as the Sn source in conjunction with the ternary solvent solution; NaBr served as an additive. As shown in Fig. 6a, the overall nanorod assemblies were square in footprint and had an average edge length of approximately 80 nm. The roughness observed at the top surface indicates that each array is composed of primary nanorod subunits with an average diameter of 10 nm, and is confirmed by TEM imaging shown in Fig. 6b. XRD and SAED results (Fig. 6b inset) can be indexed to the rutile phase of SnO_2, and confirm that the 750 nm long assemblies grew along the [0 0 1] direction. The SAED results also reveal that the square cross-sectioned mesocrystals are enclosed by (1 1 0) family planar surfaces.

Parallel striping (Fig. 6c) near the center of the nanorod assembly arises from the superposition of several primary nanorod layers, confirming the mesocrystalline qualities of the nanorod array. The clear lattice fringes seen in the

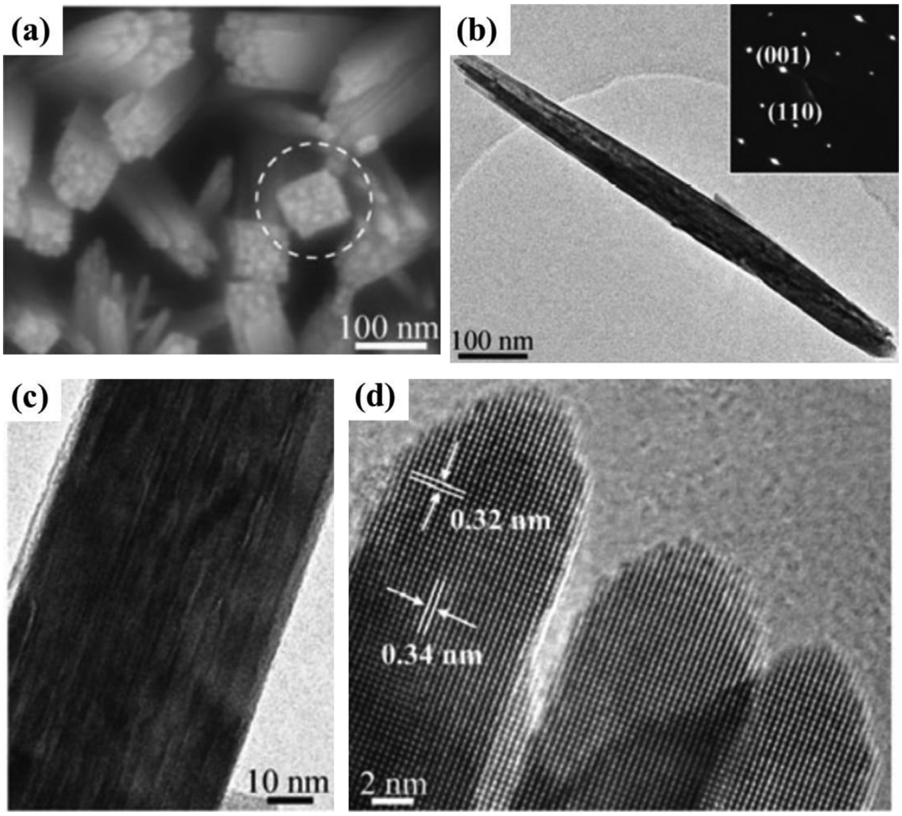

Figure 6 (a) SEM and (b—d) TEM images of mesocrystalline SnO_2 nanorod arrays grown on Ti foil. Inset in (b) is the SAED pattern of the corresponding image.
Reprinted with kind permission from Springer Science + Business Media: Nano Research, ''Kinetics-controlled growth of aligned mesocrystalline SnO_2 nanorod arrays for lithium-ion batteries with superior rate performance'', 2013, 243—252, Shuai Chen, Miao Wang, Jianfeng Ye, Jinguang Cai, Yurong Ma, Henghui Zhou, and Limin Qi, Figs. 1, 2 and 6 [110].

HRTEM image, Fig. 6d, attest to the orientation and high crystallinity of the primary nanorod subunits.

Consequently, a prospective formation mechanism was proposed for the mesocrystalline SnO_2 nanorod arrays by examining products obtained at various solvothermal reaction time intervals. The tentative, kinetics controlled, growth mechanism is depicted in Fig. 7a. By appropriately adjusting the ternary solvent ratio, the Sn(IV) hydrolysis process was controlled to allow for the heterogeneous nucleation on the substrate but reject homogeneous nucleation in solution. Following nucleation on the substrate, the surface energy of the nuclei is reduced by the adsorption of organic ligands such as HAc and ethyl acetate. These organic compounds are then incorporated into the nucleating crystals, thus forming the initial mesocrystalline nuclei. The SnO_2 nuclei continue to grow as the hydrolysis process carries on, eventually developing into the SnO_2 nanorod bundles. Following this, the SnO_2 primary nanorod subunits continue to grow along the [0 0 1] direction where the incorporated organic ligands prevent fusion of the individual subunits. In addition to Ti foil, the mesocrystalline SnO_2 nanorod arrays were also successfully deposited on fluoride-doped tin oxide (FTO), Si, graphite, and polytetrafluoroethylene (PTFE).

Following an annealing step to remove the incorporated organic species, the mesocrystalline SnO_2 nanorod arrays were electrochemically tested. When cycled at various current rates, the mesocrystalline SnO_2 nanorod array demonstrated capacities of 980, 872, and 725 mA h g^{-1} at 0.2, 5, and 10 C, respectively (1 C = 782 mA g^{-1}). Furthermore, the arrays displayed Coulombic efficiencies as high as 68, 72, and 66% during the initial cycle, respectively. These electrochemical performance values are reportedly higher than those reported for non-mesocrystalline SnO_2 nanoparticle arrays [111,112]. These performance results were ascribed to the combination of the one-dimensional nanorod and mesocrystalline structures. Specifically, the one-dimensional nanorod arrays allocate for short diffusion lengths, conductive substrate, and facile strain relaxation. Additionally, the mesocrystalline qualities impart a protective structural buffer against volume cycling, fast electron transport between neighboring primary nanorod subunits, more reactive sites, and large contact area with the electrolyte. These results clearly demonstrated that mesocrystalline SnO_2 nanorod arrays are well suited as an anode material for lithium-ion batteries.

CuO

Xu et al. developed an electrochemical synthesis route that produced leaf-like CuO mesocrystals without the aid of any surfactants [113]. Copper foils were simply immersed in an aqueous solution of $NaNO_3$ to which a constant voltage was applied. The resulting mesocrystals adopted a two-dimensional needle-like morphology, and were designated

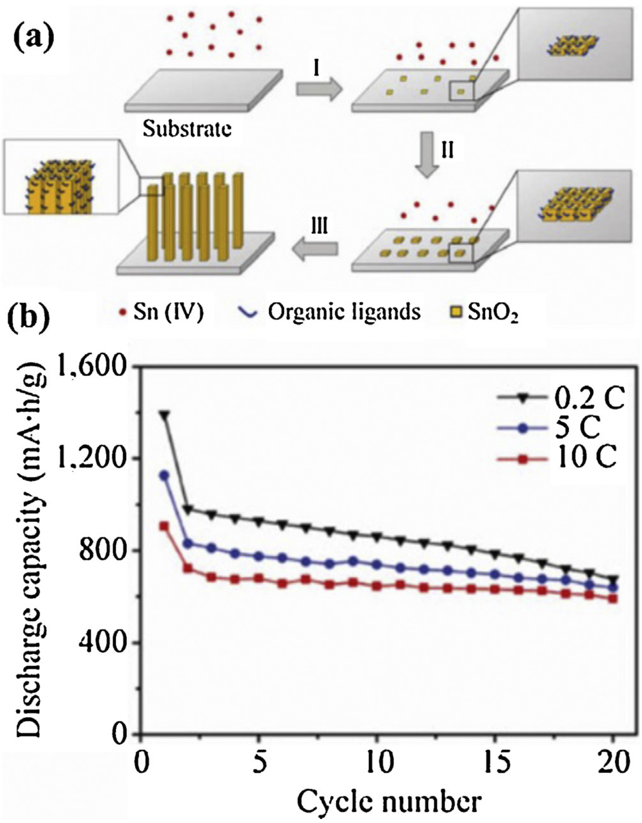

Figure 7 (a) Schematic of the proposed growth mechanism of mesocrystalline SnO_2 nanorod arrays on a given substrate; (b) cycling performance of mesocrystalline SnO_2 nanorod arrays at varying current rates.

Reprinted with kind permission from Springer Science + Business Media: Nano Research, ''Kinetics-controlled growth of aligned mesocrystalline SnO_2 nanorod arrays for lithium-ion batteries with superior rate performance'', 2013, 243—252, Shuai Chen, Miao Wang, Jianfeng Ye, Jinguang Cai, Yurong Ma, Henghui Zhou, and Limin Qi, Figs. 1, 2 and 6 [110].

'nanoleaves', as shown in Fig. 8a. The CuO nanoleaves were approximately 50 nm wide and several hundreds of nanometers long. Moreover, the nanoleaves were composed of many small particles (Fig. 8b). Fig. 8c displays an HRTEM image of a single nanoleaf, while Fig. 8d reveals the corresponding SAED pattern. The single crystal like quality of the SAED pattern indicates that the nanoparticles making up the nanoleaf share the same crystallographic orientation. Time resolved deposition/growth analysis uncovered that the CuO mesocrystals form through the oriented attachment of small nanocrystals. It is speculated that the CuO mesocrystals formed through the dehydration of $Cu(OH)_2$, and subsequently self-assembled along a mutual orientation. The leaf-like morphology was adopted because of defects and surface energy constraints, which lead to different growth rates along the width and length of the nanoleaves. However, a more lucid and detailed formation mechanism has yet to be divulged.

Upon investigating the electrochemical performance of the CuO mesocrystal, it was established that the CuO mesocrystals exhibit a high initial discharge capacity of 1063 mA h g^{-1} and a reversible capacity of 674 mA h g^{-1}, which is close to the theoretical capacity of 670 mA h g^{-1} as shown in Fig. 8e. The cycle stability is also displayed in Fig. 8e, and a slight capacity fading was observed over the course of 30 cycles. Comparatively, the CuO microflake electrode deteriorated quite quickly and had a reversible capacity less than 200 mA h g^{-1} after 30 cycles. The improved electrochemical characteristics of the CuO mesocrystalline nanoleaves were ultimately attributed to their high surface area, confined thickness, and oriented single crystal domains.

Fe_2O_3

α-Fe_2O_3 (hematite) is a rhombohedrally centered hexagonal structure of corundum with a close-packed oxygen lattice in which two-thirds of the octahedral sites are occupied by Fe^{3+} ions, and is the most stable iron oxide under ambient atmosphere. Utilizing hydrothermal techniques, An et al. were able to synthesize monodisperse elliptic α-Fe_2O_3 superstructures from nanorod primary units without the use of any template or organic surfactant [114]. More specifically, the hydrothermal process only involved ferric chloride and water. The morphology of the hematite mesocrystals could be adjusted from spherical, nanosheet-based to quasi spindle-like, block-shaped by slightly adjusting the solvent of the reaction system. The elliptically shaped material had an average center diameter of 2 μm and length of 3 μm. The SEM image of a single α-Fe_2O_3 superstructure indicates the rod-assembled nature of the sample (Fig. 9) made up of α-Fe_2O_3 nanorods with an average diameter of 40 nm and length of 200 nm.

The proposed formation mechanism behind the fabrication of these α-Fe_2O_3 assemblies was constructed based on the products observed with SEM at staged reaction intervals. It was suggested that the initial nucleation of iron oxide nanocrystals from solution was followed up by the formation of rod-like nanocrystals through oriented attachment under the influence of the dipole interactions and the thermodynamic driving force. These nanorods eventually assembled into quasi urchin-like structures by oriented attachment, and the elliptic mesocrystals were formed when adjacent nanorods rotated in an attempt to share the same crystallographic orientation. The alignment of the nanorods with respect to one another is thermodynamically favored because the surface energy is reduced when the interfaces are eliminated. Incorporation of ethanol as solvent during the hydrothermal growth process had tremendous impact on the final mesocrystal morphology, and it was reasoned that ethanol induces the production of an iron alkoxide precursor. When cycled in the voltage range of 0.5—3.0 V and at a current density of 0.2 mA cm^{-2}, the α-Fe_2O_3 material demonstrated a flat discharge profile and an initial capacity of 840.1 mA h g^{-1}. Unfortunately, cycle stability was not examined and compared to that of α-Fe_2O_3 nanoparticles under analogous conditions.

Duan et al. expanded on this initial finding by developing rhombic and ellipsoidal α-Fe_2O_3 mesocrystals from the solvothermal reaction of iron (III) nitrate nonahydrate in a solution of dimethyl formamide (DMF) and methanol (Fig. 10) [115]. The rhombic and ellipsoidal α-Fe_2O_3 mesocrystals had a characteristic overall assembly size of 200 and 400 nm, respectively, but were both built

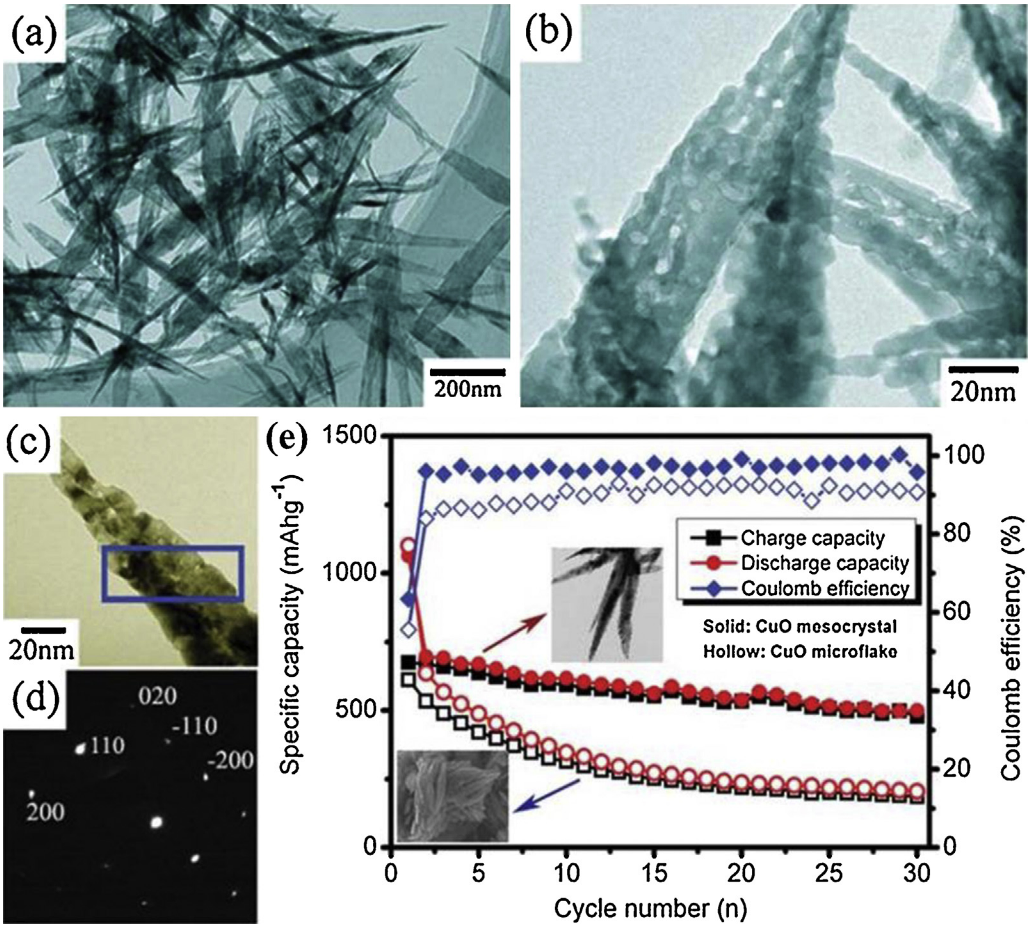

Figure 8 TEM images of the leaf-like CuO mesocrystals at (a) low and (b) high magnification; (c) TEM image and (d) SAED pattern (from the highlighted area) of an individual CuO nanoleaf. (e) The cycle performance of the leaf-like CuO mesocrystal compared with CuO microflake.
Reproduced from Ref. [113] with permission from The Royal Chemistry Society.

from nanosized subunits with diameters around 10 nm. Decreasing the amount of DMF during synthesis resulted in insufficient $NH_2(CH_3)_2$ to coat and stabilize the primary particle high-energy facets during growth, while more methanol would accelerate Fe^{3+} hydrolysis by the esterification reaction. Both the rhombic and ellipsoidal α-Fe_2O_3 mesocrystals were cycled against lithium within the voltage range of 0.5—3.0 V and at a current density of 100.7 mA g^{-1}. After 50 cycles, the rhombic mesocrystals stabilized at approximately 756 mA h g^{-1} while the porous α-Fe_2O_3 ellipsoidal mesocrystal had a capacity of 512 mA h g^{-1}. These findings further validate the positive effects mesocrystals can have over nanoparticles from an electrochemical energy storage perspective.

Positive electrode materials

Compared to their anodic partners, there are considerably fewer studies concerning cathodic electrode materials; it is probably attributable to the fact that cathodic materials are typically complex oxides. The synthesis of nanostructured primary units and crystallographic alignment of complex oxides are understandably more challenging and difficult to control. Specifically, it is common for cathodic materials to contain lithium in the as-prepared state. Provided the qualities of lithium, its stoichiometry under most synthetic processing methods is problematic to govern. On the industrial level, cathode materials are prepared by adding a lithium compound to a mixed transition metal hydroxide and then calcining at high-temperature. Regardless, several studies focusing on the synthesis and performance of mesocrystalline materials as cathode in lithium-ion batteries have already been reported. The physical and electrochemical characteristics of these systems have been compiled and are shown in Table 2. Upon comparing Tables 1 and 2, it is evident that the overall size of all cathode mesocrystals is substantially larger than the anode mesocrystals; the reason behind this is currently unknown but may be worth exploring moving forward.

V_xO_y

Monoclinic nanostructured metastable vanadium dioxide, $VO_2(B)$, was synthesized from the reduction of commercially available V_2O_5 utilizing additive-free solution-based processing methods where oxalic acid served as both the reducing and chelating agent due to its disposition to serve

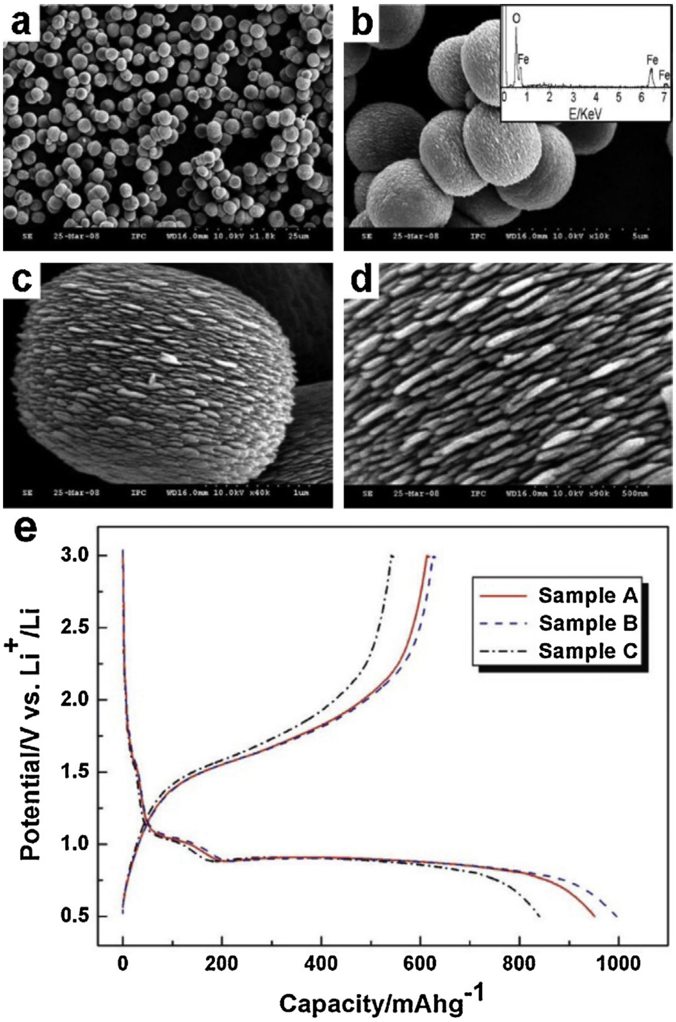

Figure 9 (a—d) SEM images and (e) first charge-discharge profile curves of elliptic α-Fe_2O_3 mesocrystals. Inset in (b): EDX spectrum of the sample.
Reprinted with permission from An et al., J. Phys. Chem. C, 2009, 113, 8092—8096. Copyright 2009 American Chemical Society [114].

as a bidentate ligand [116]. The size and morphology of the as-prepared VO_2(B) material was examined using SEM, the results of which are displayed in Fig. 11a. A typical VO_2(B) sample was mainly composed of uniform micron sized ellipsoidal stars with an average height and width of approximately 2.8 μm and 1.5 μm, respectively. Each mesocrystal was composed of six arms that are self-assembled from stacked nanosheets 20—60 nm thick and radially aligned

Table 2 Summary of physical and electrochemical characteristics of mesocrystalline cathode materials.

Reference	Material	Phase	Overall morphology	Overall size (nm)	Subunit morphology	Subunit size (nm)	Initial capacity (mA h g^{-1})
[116]	VO_2(B)	Monoclinic	Microstar	2800	Sheet	40	259(1 C)
[123]	V_2O_5	Orthorhombic	Hollow sphere	2000	Rod	200	286 (1 C)
[125]	$LiMn_2O_4$	Spinel	Rhombohedral	10,000	Plate	500	98 (1 C)
[126]	$LiMn_{1.5}Ni_{0.5}O_4$	Spinel	Cube	10,000	Sheet	200	127 (0.1 C)
[126]	$LiMn_{1.5}Ni_{0.5}O_4$	Spinel	Sphere	15,000	Particle	200	129 (0.1 C)
[128]	$LiFePO_4$	Olivine	Disk	1000	Particle	100	150 (2 C)
[129]	$LiFePO_4$	Olivine	Spindle	1000	Particle	50	157 (0.1 C)
[131]	$LiFcPO_4$	Olivine	Dumbbell	2000	Plate	50	100 (0.3 C)

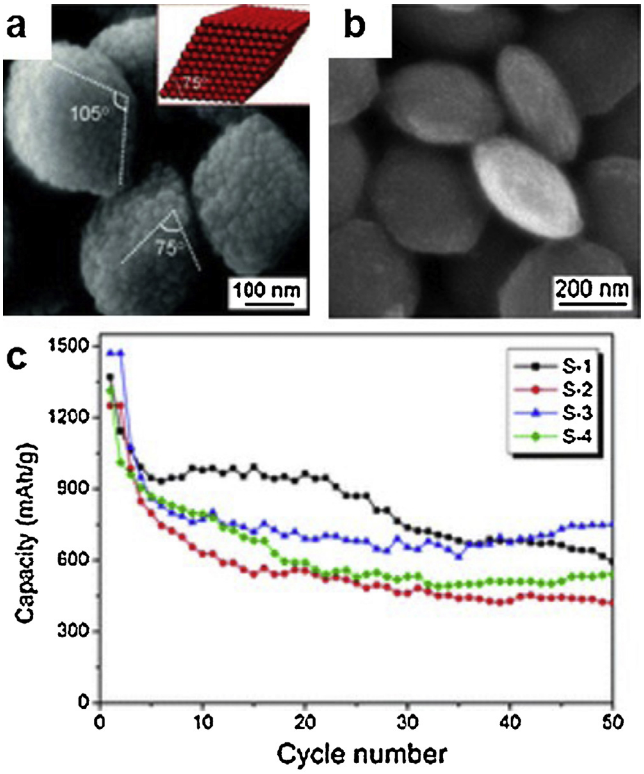

Figure 10 Representative morphologies of the as-synthesized hematite mesocrystals from different solvent mixtures: (a) rhombic mesocrystal (S-3) when (DMF): $(CH_3OH) = 20:5$ and (b) ellipsoidal mesocrystal (S-4) when $(DMF):(CH_3OH) = 18:7$. Discharge cycling performance of the electrode made from the as-prepared α-Fe_2O_3 nanostructures with different morphologies in the voltage range of 0.05—3.0 V at a current rate of 0.1 C.
Reproduced from Ref. [115] with permission from The Royal Chemistry Society.

with respect to the center of the structure. Cross-sectional TEM images of an ultramicrotomed sample (Fig. 11b and c) approximate the overall thickness of each hierarchically nanostructured arm at 200—300 nm. The inset of Fig. 11c displays the SAED pattern for an arm region, the single crystalline nature of which confirms mesocrystal formation. Indexing the SAED pattern revels that the individual VO_2(B) nanosheets exhibit preferential growth along the [0 1 0] direction, indicating that the (0 1 0) plane has a relatively high stacking rate and is realized by considering the relative stacking rate of the octahedra at various crystal faces [117].

Although the exact formation mechanism is not entirely clear, a proposed formation mechanism is illustrated in Fig. 11d. The proposed formation pathway initiates with nanobelts that were directly observed several hours into the solvothermal treatment. The nanobelts in solution will coarsen and grow into ellipsoidal nanosheets through classical crystal growth methods. It is likely that the precursor vanadium oxalate is synthesized as an intermediate during the reaction as the conjugate base of oxalic acid, oxalate, is an excellent ligand for metal ions and usually binds forming a five-membered MO_2C_2 ring. The presence of the chelating agent should modify the surfaces of the growing nanocrystals, particularly the surfaces that possess the lowest electronic density, thus leading to the growth of specific surfaces and aiding in the synthesis of the observed micro-architectured nanosheet morphology. The [0 1 0] growth direction of the nanobelts is maintained during this step, as determined from SAED [117—119]. Several nanosheets then stack homoepitaxially over one another in order to minimize the energy of the system. Residual chelating agent remaining on the (1 0 0) surface of each nanosheet effectively decreases the Debye length of the electric double layer and stabilizes the van der Waals forces of the constituting components, leading to superstructure formation while preventing fusion between individual nanosheets [120]. These stacked VO_2(B) nanosheets will coalesce together to form the star-like architecture through the oriented attachment mechanism [85].

The rate capability of the VO_2(B) mesocrystals was tested at incremental discharge rates, for 15 cycles at each increment, starting at 150 mA g^{-1} (1 C) and terminating at 1500 mA g^{-1}, the results of which are displayed in Fig. 11d. Most notably, the VO_2(B) electrodes demonstrated a high capacity of 158 mA h g^{-1} at the 10 C rate. Cycle stability investigation at the 1 C rate determined that the VO_2(B) electrodes adopt a stable capacity value of approximately 195 mA h g^{-1} up to fifty cycles. In essence, it was concluded that the exceptional capacity of the VO_2(B) superstructures can be attributed to the mesocrystalline arrangement that leads to the exposure of the (0 0 1) facet, which have a lower energy barrier for faster and more efficient Li-ion intercalation [121,122].

In addition to VO_2(B) mesocrystals, Cao et al. synthesized hollow V_2O_5 microspheres composed of nanorods *via* self-assembly [123]. Hollow microsphere precursors of vanadyl glycolate composed of assembled nanorods were first synthesized utilizing the polyol process, and were then transformed to V_2O_5 with a simple annealing step. No change in the morphology was observed upon annealing. The individual nanorods comprising the structure were approximately 200 nm in diameter and varied in length, while the overall spherical structures were approximately 2 μm in diameter. The structures were successfully able to intercalate up to one Li^+ per V_2O_5 formula unit, and showed moderate capacity retention up to 15 cycles with an initial discharge capacity of 286 mA h g^{-1} [123]. It was determined that interconnecting nanoparticles between the self-assembled nanorods lead to a reduction in the Li^+ diffusion distance, thereby increasing the kinetics of the material and the overall electrochemical performance. It has since been revealed that hollow structures can result in favorable enhancements in capacity retention with cycling due to the presence of the inner cavity that can accommodate cycling induced strain due to the de/intercalation of Li^+ [124].

$LiMn_2O_4$

Dang et al. established a selective mesocrystal formation methodology for various manganese oxides based on the topotactic transformation of a biomimeticaly prepared $MnCO_3$ precursor through an Mn_5O_8 intermediate [125]. The term topotaxy describes all solid state reactions that lead to a material with respective crystal orientation that

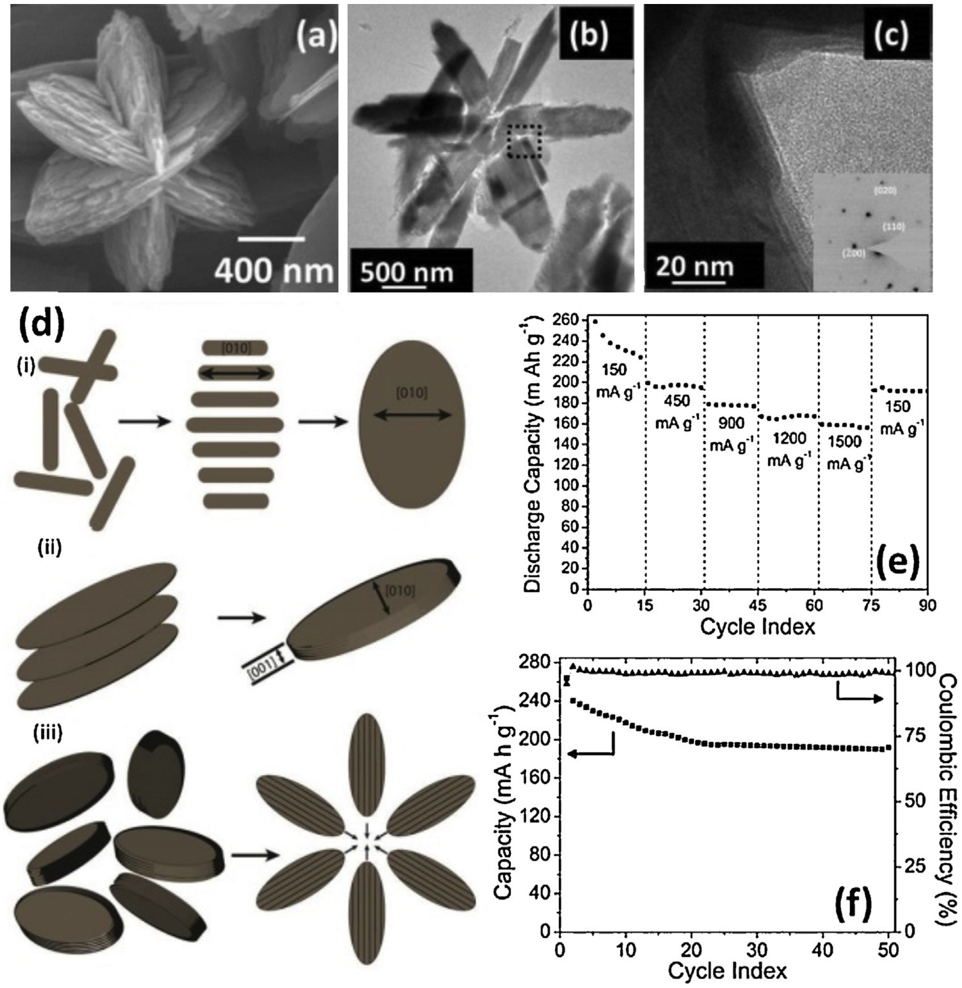

Figure 11 (a) Representative SEM image of the as-synthesized vanadium dioxide mesocrystals showing the stacked nanosheets composing each arm; (b and c) TEM images of a cross-sectioned VO_2(B) mesocrystal and corresponding SAED pattern (inset). (d) Proposed formation mechanism of the VO_2(B) mesocrystals; (e) discharge-rate capability at various current densities and (e) cycle stability and Coulombic efficiency over 50 cycles at 150 mA g^{-1}.
Reprinted with permission from Uchaker et al., Small 2013, 22, 3880—3886. Copyright 2013 John Wiley & Sons, Inc. [116].

can be correlated with crystal orientations in the initial product [11]. In brief, the mesocrystalline $MnCO_3$ precursor was annealed to form the Mn_5O_8 intermediate, while the mesocrystal morphology was maintained, and was then reacted hydrothermally with LiOH to form the various mesocrystalline Li—Mn—O compounds. The initial $MnCO_3$ precursor took on a rhombohedral morphology with an edge length of approximately 10 μm. The subunit particles that made up the $MnCO_3$ precursor were square, uniform platelets approximately 500 nm in size, as revealed in Fig. 12a and b. The precursor morphology and subunit particle size was preserved during the intermediate Mn_5O_8 topotactic transformation process; however, pores with an average size of 100 nm were formed due to the decomposition of $MnCO_3$, specifically the volume reduction attributed to the removal of CO and CO_2 (Fig. 12c and d). More notably, different Li—Mn—O compounds could be acquired by adjusting the quantity of LiOH used during the hydrothermal process — specifically, $LiMnO_2$, $LiMn_2O_3$, and $LiMn_2O_4$. Too high of annealing temperature resulted in a randomly oriented Mn_2O_3 product which also failed to adopt nanoparticle orientation following hydrothermal treatment. A schematic diagram of the various formation pathways is illustrated in Fig. 12e.

The shape and size of the overall $MnCO_3$ precursor was maintained through the hydrothermal process, and imparted unto the $LiMnO_2$, $LiMn_2O_3$, and $LiMn_2O_4$ products. However, the size and morphology of the subunit nanoparticles comprising the superstructures differed significantly, as can be observed in Fig. 13a—d. For instance, $LiMn_2O_4$ prepared with only 12 wt% more LiOH exhibited both nanosheet and nanoparticle morphology with average sizes of 100 and 250 nm, respectively. The packing density and surface roughness of the mesocrystal composing nanoparticles could also be tailored by adjusting the amount of LiOH used, based on SEM images.

The lithium intercalation capability of the $LiMn_2O_4$ mesocrystals were then investigated, and compared to that of porous, single-crystalline $LiMn_2O_4$ nanoparticles. The typical two-stepped plateau of the $LiMn_2O_4$ cubic spinel,

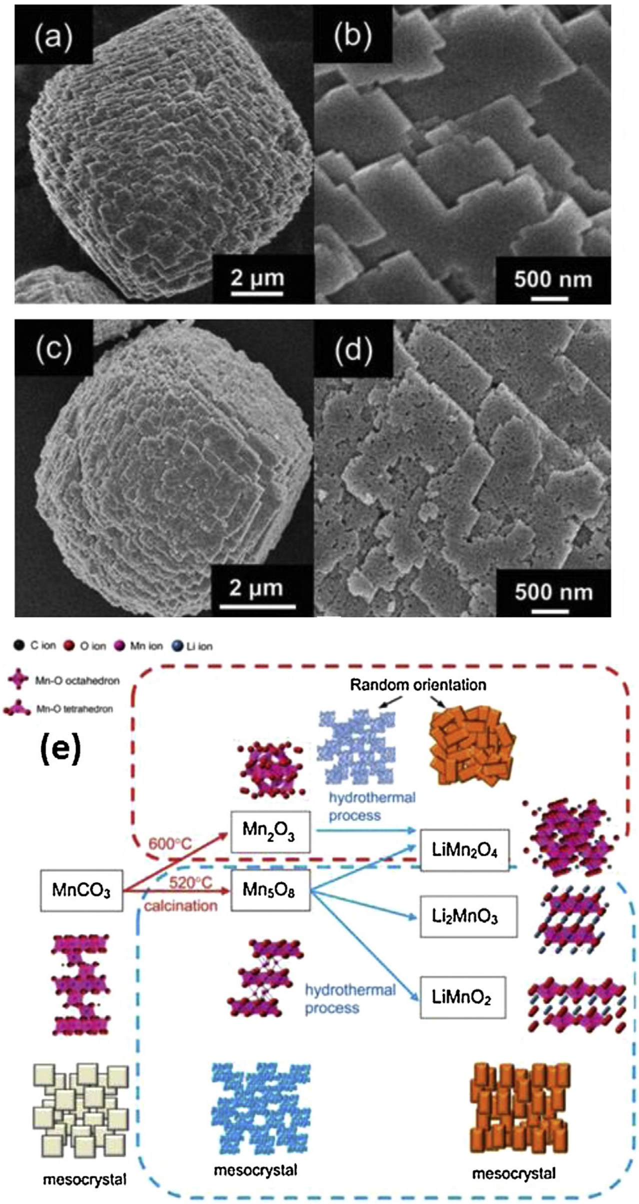

Figure 12 SEM images of the (a and b) $MnCO_3$ and (c and d) Mn_5O_8 precursor mesocrystals. (e) Transformation from $MnCO_3$ precursors to lithium manganates *via* manganese oxides where the final crystal phase depends on the [LiOH]/[Mn_5O_8] molar ratio during the hydrothermal process.
Reproduced from Ref. [125] with permission from The Royal Chemistry Society.

corresponding to two different Li-ion intercalation processes, was obtained, and the specific capacity was 98 mA h g^{-1} at 100 mA g^{-1}. It is worth mentioning that the half-cells were cycled between 3.1 and 4.4 V, which is a relatively large electrochemical window. A comparison of the capacity retention of the $LiMn_2O_4$ mesocrystals and randomly oriented nanoparticles, when cycled at 100 mA g^{-1}, is shown in Fig. 13e. After 100 cycles, the mesocrystalline $LiMn_2O_4$ retained 86% of its initial capacity, while the nanoporous specimen was only able to maintain 74% of its preliminary value. Additionally, a composite electrode prepared from equal parts $LiMnO_2$ and $LiMn_2O_3$ demonstrated exemplary capacity at various current densities, most notably 192 mA h g^{-1} at 10 mA g^{-1}. The enhanced electrochemical performance of the mesocrystals was attributed to their high degree of crystallinity and exposure of specific surface facets.

$LiMn_{1.5}Ni_{0.5}O_4$

Cao et al. successfully developed an approach to regulate the morphology of Mn and Ni based carbonate precursors. Highly uniform and oriented particulate assemblies yielded well-designed superstructures with high tap density and high voltage capability [126]. $LiMn_{1.5}Ni_{0.5}O_4$ (LMNO) adopts the spinel structure while offering a high operating voltage and rate capability, but its morphology is difficult to control because of the high synthesis temperatures often required. Manganese and nickel containing carbonates were effectively synthesized by exploiting the gradual production of NH_3 and CO_2 stemming from the decomposition of urea during hydrothermal treatment.

The morphology was controlled by using different salt compounds; Fig. 14a and c shows the carbonate based Mn and Ni precursors formed using metal chlorides and metal sulfates, respectively. The inset picture of Fig. 14a clearly demonstrates that the mesocrystalline microcube had an edge length of approximately 10 μm and a tap density as high as 1.7 g cm^{-3}. Closer inspection reveals that the microcubes are in fact built up from layers of oriented and stacked square nanosheets approximately 200 nm in dimension. Time resolved hydrothermal growth investigations suggested that $MnCO_3$ precipitated out preferentially, and that the Ni^{2+} ions took some time to fully precipitate into $NiCO_3$. However, the full precipitation of $NiCO_3$ coincided with radical change in the sample morphology from random and irregular to oriented and hierarchical. The carbonate based microspheres, Fig. 14c, had an average diameter of 15 μm but were also composed of nanoparticle subunits, albeit less uniform than the microcube counterpart. As expected, based on geometrical considerations, the microspheres had a higher tap density of 1.9 g cm^{-3}.

Elemental mapping of each morphology proved that $MnCO_3$ and $NiCO_3$ were successfully co-precipitated throughout each particle; no detectable degree of segregation was noticed. XRD confirms the presence of $MnCO_3$ and $NiCO_3$ in both the mesocrystalline microcubes and microspheres, although the peaks are more intense for the microcubes indicating a higher degree of crystallinity. The narrow size distribution of both the superstructure morphologies is ascribed to Ostwald ripening. Heat treatment of these materials with LiOH generated LMNO.

The electrochemical performance of the LMNO mesocrystals was compared to that of irregularly shaped, commercially available material when cycled between 3.4 and 5 V. Fig. 14e reveals that both the mesocrystalline microspheres and microcubes exhibited superior cycle stability with essentially no capacity fade over fifty cycles; the commercial LMNO sample demonstrated moderately lower initial capacity and experienced an 11% capacity fade under the same conditions. It is possible that the improvement in cycle stability might be attributed to the uniformity in particle size and geometrical robustness of the mesocrystal particles. Overall, the study validated the superiority of the mesocrys-

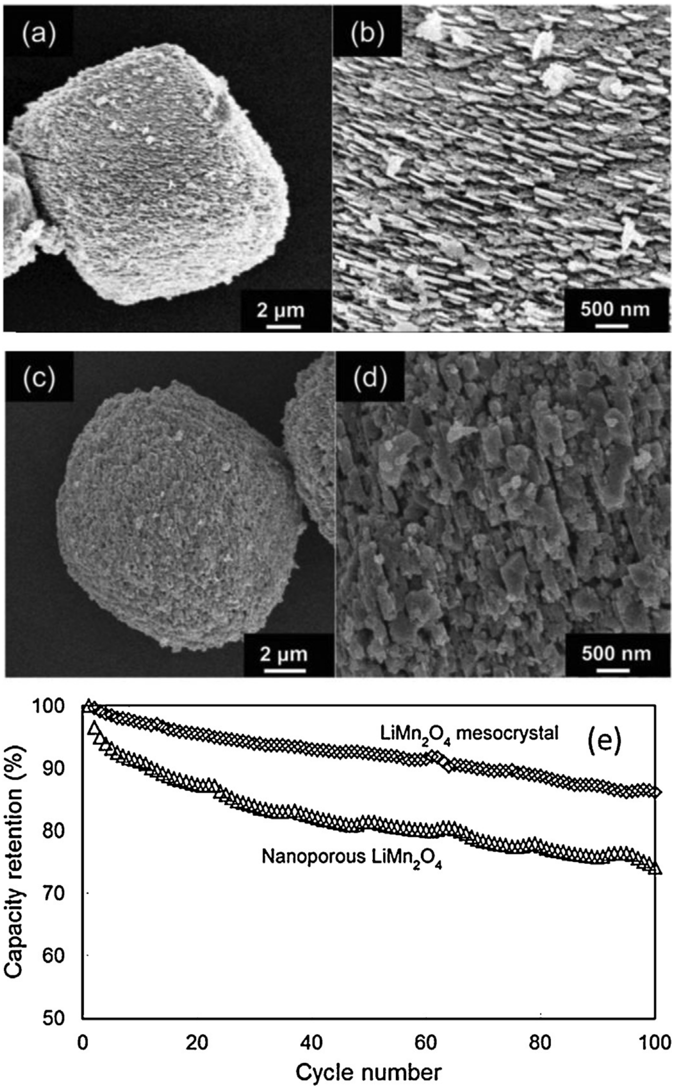

Figure 13 SEM images of $LiMn_2O_4$ prepared at a $LiOH/Mn_5O_8$ molar ratio of (a and b) 7/1 and (c and d) 8/1. (e) Cycle stability in terms of capacity retention for the $LiMn_2O_4$ mesocrystals from (c and d) compared with nanoporous $LiMn_2O_4$ particles between cutoff voltages of 3.1—4.4 V and at a current density of 100 mA g^{-1}.
Reproduced from Ref. [125] with permission from The Royal Chemistry Society.

tal materials in terms of higher volumetric capacity and stability.

$LiFePO_4$

Lithium iron phosphate ($LiFePO_4$ or LFP) has attracted much attention in both research and industrial communities because of its high theoretical capacity of 170 mA h g^{-1}, stable discharge rate at a voltage of ~3.4 V, low cost due to abundance of raw materials, and excellent thermal and chemical stability [127]. Yet, LFP has despairingly low electrical conductivity that limits its application in high power devices but could potentially be mitigated by the use of mesocrystalline electrode materials. Bilekca et al. synthesized $LiFePO_4$ mesocrystals *via* an extremely efficient microwave-assisted route [128]. The versatility of this synthesis method was illustrated by its ability to synthesize $LiMnPO_4$ under similar conditions. Fig. 15 portrays the as obtained product which was composed of slightly elongated nanoparticles (~100 nm) nearly fused together into disks approximately 1 μm in diameter. The LFP mesocrystals were tested as cathode material for Li-ion battery, and exhibited an initially moderate capacity of 150 mA h g^{-1} that was extremely stable upon cycling when cycled from 2.0 to 4.5 V at a rate of 340 mA g^{-1} (2 C). The LFP mesocrystals also show modest rate capability (81%) up to a discharge rate of 8 C. Despite the lack of a carbon coating and modest cycling performance, the study did not clarify or expand upon the relationship between the unique structural features and the performance of the LFP mesocrystals and only suggested that the implementation of mesocrystals as electrode material may be the linking factor [128].

In an attempt to compensate for the low electronic conductivity of LFP, carbon coated LFP mesocrystals were later studied by Xia et al., where they were synthesized using a solvothermal and post-growth annealing route [129]. A nearly identical technique [130], except for the inclu-

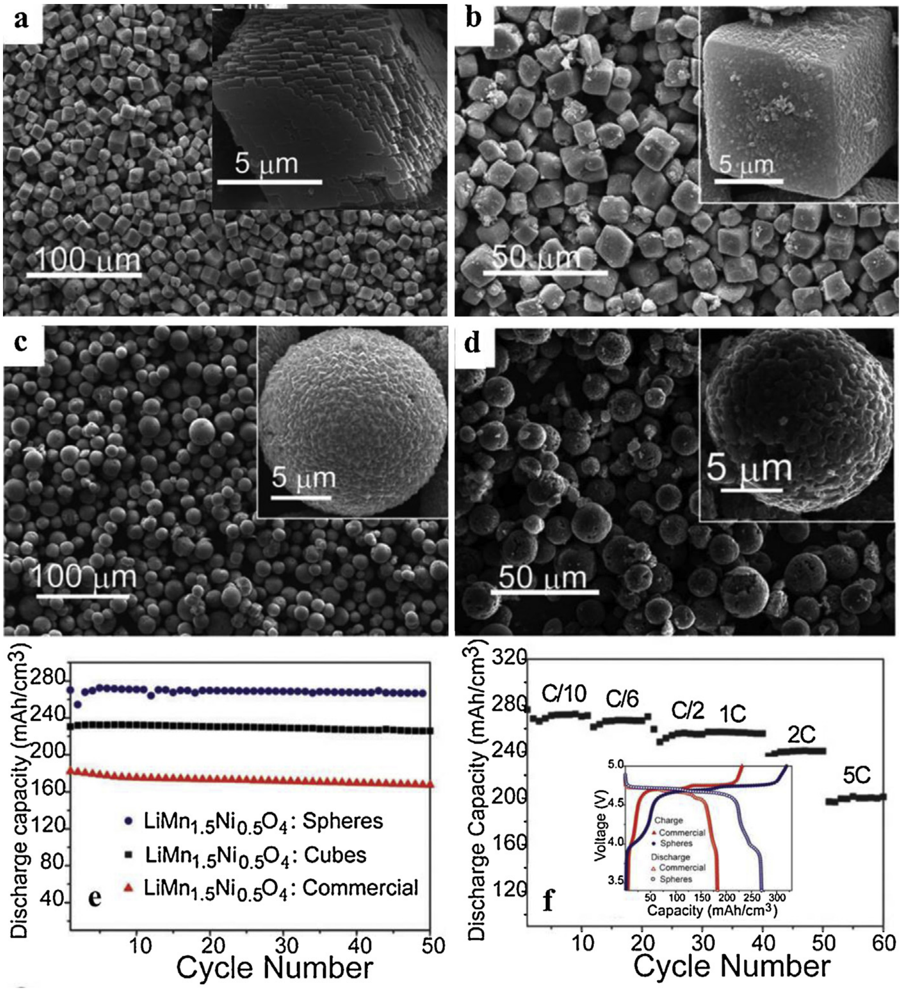

Figure 14 SEM micrographs of mesocrystalline microcube (a) carbonate precursor and (b) LMNO final product; mesocrystalline microsphere (c) carbonate precursor and (d) LMNO final product. (e) Comparative cycle performance of LMNO mesocrystalline microcubes, microspheres, and commercial nanoparticles. (f) Rate capability of $LiMn_2O_4$ mesocrystalline microspheres; inset: first dis/charge profiles of the LMNO mesocrystalline microcubes, microspheres, and commercial nanoparticles at the 0.1 C current rate. Reproduced from Ref. [126] with permission from The Royal Chemistry Society.

sion of surfactant during synthesis, that yielded analogous product has been reported by Chen et al. The annealing route was required in order to convert the L-ascorbic acid into the carbon that coated the surface of the primary nanoparticles. In this way, the carbon coating encasing all of the nanoparticle primary subunits was uniform and the mesocrystal structure itself provided a framework for improved conduction. Spindle-like structures approximately 2 μm in length and 1 μm in width, composed of nanoparticles approximately 100 nm in length and 50 nm in width, were observed with SEM and are depicted in Fig. 16. TEM analysis revealed the mesocrystalline nature of the obtained product; it was determined LFP was formed almost immediately during reaction and that the morphology progressed through standard non-classical crystallization techniques using a nanoparticle surface modifier as determined from time dependent growth studies.

The spindle-like LFP mesocrystals demonstrated an incredibly stable cycling stability of approximately 157 mA h g^{-1} over the course of 50 cycles at the 0.1 C rate, with an overall drop in capacity of only 3%. Conversely, electrochemical impedance spectroscopy revealed that the charge transfer resistance (R_{ct}) decreased from 57.7 Ω to 28.7 Ω after the 50 cycles; the LFP mesocrystals also exhibited a moderate rate capability that terminated at 117 mA h g^{-1} at a rate of 5 C (Fig. 16d). The electrochemical performance was attributed to the porous structure that shortened the Li^+ diffusion length, enhanced electrolyte penetration, and increased the electrochemical reaction surface, thus alleviating electrode polarization. The incorporation of the uniform carbon coating throughout the structure also aided the electrochemical capability by enhancing the electronic conductivity.

In a separate study, $LiFePO_4$ samples with dumbbell-like mesocrystals, as shown in Fig. 17, were prepared by a simple solvothermal process in the presence of polyvinyl propylene (PVP) [131]. SEM imaging shows that the dumbbell-like microstructures have length ranging from 1.5 to 2 μm and that they are hierarchically constructed with two-dimensional nanoplates that are approximately 300 nm in length and 50 nm thick. Without PVP, irregular and non-uniform plates with a large size were formed; reduced

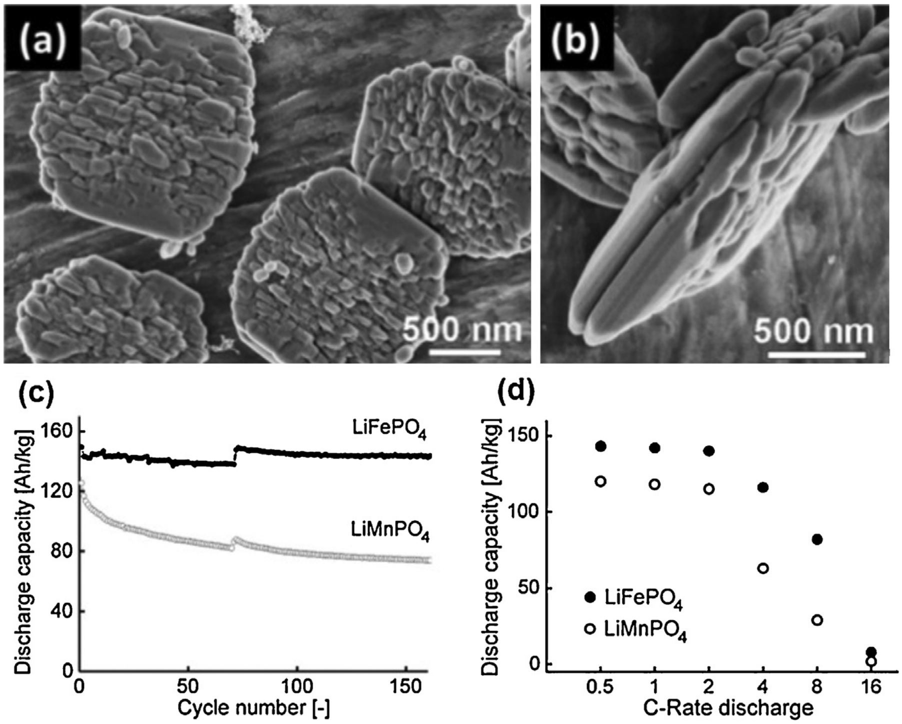

Figure 15 SEM images of $LiFePO_4$ (a) top-view and (b) side-view. (c) Cycle stability and (d) rate performance of the $LiFePO_4$ ($1\,C = 170\,mA\,g^{-1}$) and $LiMnPO_4$ ($1\,C = 150\,mA\,g^{-1}$) electrodes.
Reproduced from Ref. [128] with permission from The Royal Chemistry Society.

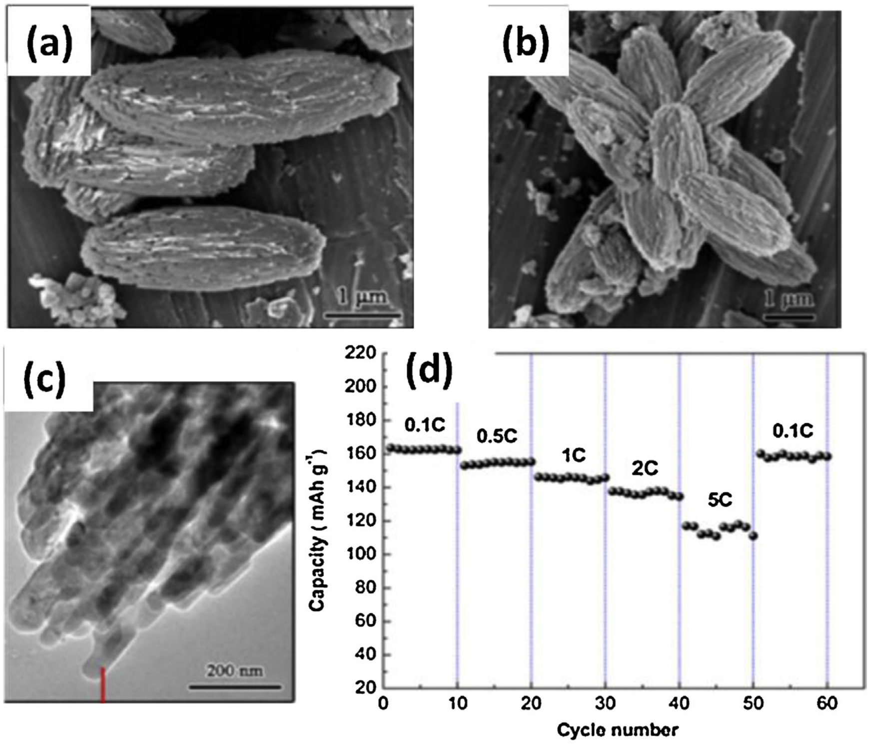

Figure 16 SEM of spindle-like LFP structure obtained over a growth period of (a) 20 h and (b) pH of 10; (c) HRTEM image. (d) The charge/discharge profiles of the spindle-like LFP architecture in the voltage range from 2.5 to 4.2 V at various current rates.
Reproduced from Ref. [129] with permission from Elsevier.

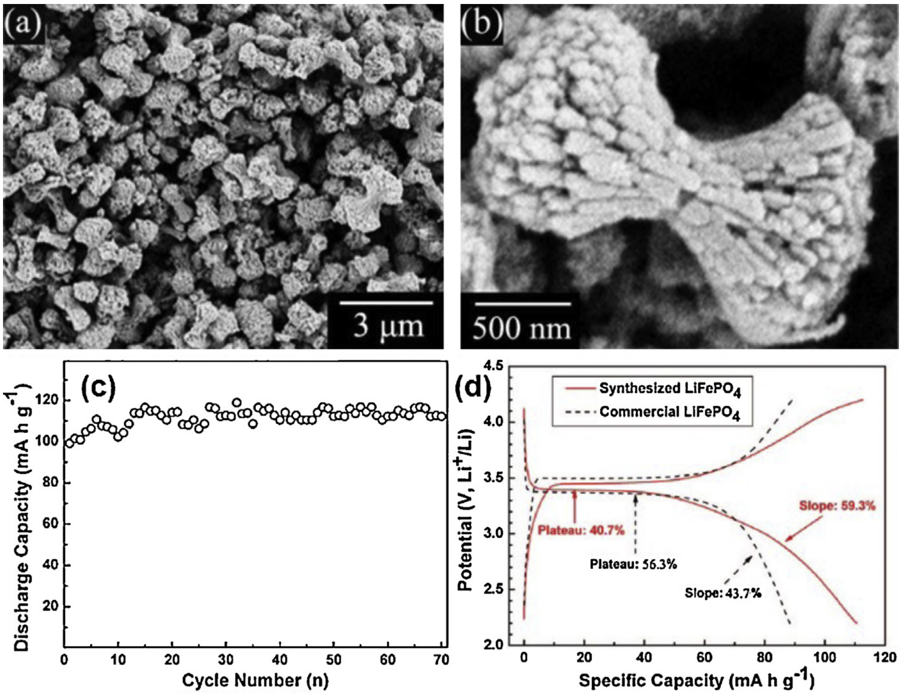

Figure 17 (a and b) SEM images, (c) cycle stability, and (d) comparison with commercially available material of the $LiFePO_4$ dumbbell-like mesocrystals.
Reprinted with permission from Yang et al., J. Phys. Chem. C 2009, 113, 3345—3351. Copyright 2009 American Chemical Society [131].

amounts of PVP resulted in three-dimensionally hierarchical microstructures formed from nanoplates, but with a wide size distribution. Synthesis with other surfactants failed to produce oriented LFP mesocrystals but rather irregular and non-uniform disk-like particles of large size.

On the basis of TEM time dependent investigations, a formation mechanism behind the dumbbell shaped LFP mesocrystals was proposed. The process was stated to carry out over several different stages that started with initial nucleation and growth of rectangular nanocrystals that would then aggregate and orientedly attach into large rectangular shaped structures due to PVP related effects. With prolonged reaction time the previously formed structures consisting of nanoplates demonstrated a preference to tilt at both ends because of lattice tension or surface interaction in the edge areas, resulting in the formation of the bowed-out assembly. Li_3PO_4, whose presence was detected using XRD, would then dissolve and recrystallize to $LiFePO_4$ where it would collect on the edges of the pre-existing $LiFePO_4$ nanoplates. Thus, is can be surmised that dumbbell $LiFePO_4$ mesocrystal formation is based on a dissolution-recrystallization process with eventually complete phase transformation.

Prior to electrochemical testing, the PVP was converted to carbon through annealing; the inherent amount of carbon present was measured to be 1 wt%. At a current rate of 0.03 C, the dumbbell mesocrystals had an initial discharge capacity of 100 mA h g^{-1} that improved to 110 mA h g^{-1} after 70 cycles. The lack of capacity fade indicates that the material is extremely stable. The capacity of the dumbbell mesocrystals was also higher than that of commercially available LFP while showing less polarization and a longer discharge plateau (Fig. 17d). The authors reasoned that the disparity between the two materials may exist because of a pseudocapacitive effect in the mesocrystalline LFP imparted by its nanosized component. Similarly shaped $LiFePO_4$ mesocrystals formed through several other routes have been reported as well [132,133].

Additional applications of mesocrystals

By no means are mesocrystals limited to energy storage applications. Several review articles summarizing the applications of mesocrystals as demonstrated experimentally have been compiled and mainly focus on their use as catalysts, sensors, optoelectronics, and biomedical applications [80,132,134].

The performance of a catalytic process corresponds directly to the adsorption and desorption of reactant molecules on the catalyst surface. Mesocrystals are ideally suited for such application because of their high surface area and inherent porosity that provide more active sites for reactant molecules to interact. The controlled exposure of catalytically active surface facets has the potential to further improve performance. A high degree of crystallinity is also often desired for catalytic applications as to achieve more efficient electron transfer and make the overall reaction process more homogeneous. CoO/ZnO nanocomposites based on CoO mesocrystal cores with a ZnO nanoparticle overlayer were successfully able to catalyze the oxidation reaction of CO to CO_2 [135]. Considerably more work has been done using mesocrystals as photocatalysts. Anatase TiO_2 mesocrystals showed good capability for enzyme immobilization and photocatalytic degradation of contaminants, validating their potential for such applications [136,137]. Many other studies examining the overall improved photocatalytic activity when compared to commercially available TiO_2 nanoparticles as well as against NO and Rhodamine B have since been conducted [102,138—145]. Other mesocrystal based photocatalysts include $Fe_2(MoO_4)_3$, ZnO, CuO, and $SrTiO_3$ [143,146—150].

The same characteristics that make mesocrystals excellent candidates for catalysts also makes them fit for sensing applications. Reduced graphene oxide-conjugated Cu_2O nanowire and long-range ordered $W_{18}O_{49}$ mesocrystals both showed superior NO_2 gas sensing performance when compared to equivalent nanoparticles lacking mesocrystalline order [151,152]. Beyond the mesocrystal structure, the boost in sensing performance was attributed to the improved conductivity and increased number of oxygen vacancies in the respective materials. The sensing ability of Co_3O_4 octahedral mesocrystals pertaining to formaldehyde and ethanol was approximately double that of Co_3O_4 commercial product down to the 100 ppm level [153]. Porous plate like α-Fe_2O_3 with controlled facet exposure showed fast recovery times when sensing acetone, CuO mesocrystal nanosheets expressed strong ability for the electrochemical detection of dopamine, and ZnO mesocrystals showed remarkable humidity sensing capability [89,154,155].

The structural features of semiconductor materials has considerable influence on their resulting optoelectronic properties, thus making mesocrystals an intriguing candidate for such application. $AgIn(WO_4)_2$ mesocrystals synthesized by a microwave-assisted method showed white emission when excited by visible light, and the photoluminescent intensity could be controlled with the overall assembly size [156]. ZnO mesocrystalline microspheres made of hexagonal nanoplates vertically oriented with respect to a spherical core showed radioactive emission at ~0.36 THz when exposed to continuously green laser light [157]. Approximately 0.016% of incident power was converted to terahertz radiation, which corresponds to a quantum efficiency of ~33%. This high efficiency makes the ZnO microspheres competitive with the best existing terahertz-emitting materials. It was determined that the terahertz vibration mode originates from the coherent vibration of the hexagonal ZnO nanoplates comprising the microsphere, as induced by laser irradiation. Additionally, ZnO mesocrystals in the form of vertical nanowall arrays were grown on p-Si [158]. When doped with Co a well-defined rectifying behavior was exhibited; moreover, the turn-on voltage could be controlled *via* the Co^{2+} concentration.

The first reports concerning mesocrystals involved naturally occurring systems, namely biominerals deriving from coccoliths and the skeletal plates of sea urchins [159,160]. Provided this background and that biominerals serve essential functions for most living organisms, mesocrystals can have a large impact in biomedical applications. Super paramagnetic and water soluble Fe_3O_4 nanoparticles are widely used in the biomedical field as targeting transporters. Too small of particle size can lead to control issues but the super paramagnetic qualities are lost above a domain size of 30 nm [11]. Spherical Fe_3O_4 mesocrystals 30—180 nm in size made up of 6—10 nm diameter nanoparticles were able to circumvent both of these issues, clearly indicating that mesocrystals are well suited for a wide host of biomedical related applications ranging from drug delivery to magnetic resonance imaging [161]. Drug based mesocrystals show faster dissolution rates than their conventional counterparts due to the prevalence of facets in the structure, and may potentially lead to new design considerations within the pharmaceutical industry [162]. Preliminary studies have also indicated that it may be possible to one day repair tooth enamel *in vivo* using the same means as those carried out for the repair of a seashell prismatic layer [163].

Concluding remarks

Ensembles and novel arrangements of nanoparticles can collectively exhibit properties vastly different than individual nanoparticles or bulk materials. Mesocrystals are a promising class of hierarchically nanostructured solid materials that coincidently have many inherent traits that are desired for Li-ion battery electrodes. Such characteristics include: large surface area, high porosity, small primary subunit size, large overall assembly size, and high degree of crystallinity. A great deal of the research efforts, to date, concerning mesocrystals have focused on understanding their formation mechanisms, but newer works reviewing their application are starting to emerge. In terms of battery performance, the uniform pore structure inherent to mesocrystals can facilitate contact with the electrolyte thereby leading to fast Li^+ transport mechanics while at the same time accommodating lithiation induced volume expansion and particle strain giving way to improved cycling stability. The oriented arrangement of nanoparticle subunits can eliminate the grain boundaries between adjacent particles thus offering much better charge and mass transport, and ultimately better rate capability. Provided this unique combination of nanoparticle properties and order combined with a microscopic or even macroscopic size, mesocrystals have strong potential as active materials for lithium-ion battery electrodes. These assemblies possess the structural and chemical stability of microsized electrodes while exploiting the beneficial properties associated with nanosized electrodes and their large reactive surface area.

Mesocrystals have also demonstrated great potential for applications in catalysis, sensors, and electronics. Other applications are yet to be explored where huge surface area and good charge and mass transfer properties are required or the hierarchical structure can offer synergistic advantages; for example, nanostructure-based solar cells, such as dye-sensitized solar cells or quantum dots solar cells, would greatly benefit from the applications of such mesocrystals, as they would offer charge transfer properties similar to single crystals, large surface area as seen for nanoparticles, and desirable light scattering.

One of the biggest challenges in the further advancement in mesocrystal research is the lack of fundamental understanding of homoepitaxial aggregation of nanocrystals, so the rationale design and synthesis of desired mesocrystals remains as an unattained goal.

Acknowledgements

Part of this work was financially supported in part by the National Science Foundation (NSF, CMMI-1030048) and the University of Washington TGIF grant. This material is based in part upon work supported by the State of Washington through the University of Washington Clean Energy Institute.

References

[1] J.B. Goodenough, K.-S. Park, J. Am. Chem. Soc. 135 (2013) 1167.
[2] Reuters, The New York Times, 2013.
[3] R.J. Stern, Energy Policy 38 (2010) 2816.
[4] Q. Zhang, E. Uchaker, S.L. Candelaria, G. Cao, Chem. Soc. Rev. 42 (2013) 3127.
[5] R. Marom, S.F. Amalraj, N. Leifer, D. Jacob, D. Aurbach, J. Mater. Chem. 21 (2011) 9938.
[6] L. Ji, Z. Lin, M. Alcoutlabi, X. Zhang, Energy Environ. Sci. 4 (2011) 2682.
[7] Y. Wang, H. Li, P. He, E. Hosono, H. Zhou, Nanoscale 2 (2010) 1294.
[8] D. Koziej, A. Lauria, M. Niederberger, Adv. Mater. 26 (2014) 235.
[9] H. Colfen, M. Antonietti, Angew. Chem. Int. Ed. 44 (2005) 5576.
[10] M. Niederberger, H. Colfen, PCCP 8 (2006) 3271.
[11] R.-Q. Song, H. Cölfen, Adv. Mater. 22 (2010) 1301.
[12] Y.G. Guo, J.S. Hu, L.J. Wan, Adv. Mater. 20 (2008) 2878.
[13] A. Nel, T. Xia, L. Madler, N. Li, Science 311 (2006) 622.
[14] V.L. Colvin, Nat. Biotechnol. 21 (2003) 1166.
[15] F.J. Heiligtag, M. Niederberger, Mater. Today 16 (2013) 262.
[16] P.G. Bruce, B. Scrosati, J.-M. Tarascon, Angew. Chem. Int. Ed. 47 (2008) 2930.
[17] A.S. Arico, P.G. Bruce, B. Scrosati, J.-M. Tarascon, W. van Schalkwijk, Nat. Mater. 4 (2005) 366.
[18] N. Meethong, H.Y.S. Huang, W.C. Carter, Y.M. Chiang, Electrochem. Solid-State Lett. 10 (2007) A134.
[19] D. Liu, G.Z. Cao, Energy Environ. Sci. 3 (2010) 1218.
[20] P. Balaya, A.J. Bhattacharyya, J. Jamnik, Y.F. Zhukovskii, E.A. Kotomin, J. Maier, J. Power Sources 159 (2006) 171.
[21] Y. Liu, D. Liu, Q. Zhang, D. Yu, J. Liu, G. Cao, Electrochim. Acta 56 (2011) 2559.
[22] J. Cabana, L. Monconduit, D. Larcher, M.R. Palacín, Adv. Mater. 22 (2010) E170.
[23] F. Lin, D. Nordlund, T.-C. Weng, Y. Zhu, C. Ban, R.M. Richards, et al., Nat. Commun. 5 (2014).
[24] N.A. Godshall, I.D. Raistrick, R.A. Huggins, Mater. Res. Bull. 15 (1980) 561.
[25] T.D. Kaun, P.A. Nelson, L. Redey, D.R. Vissers, G.L. Henriksen, Electrochim. Acta 38 (1993) 1269.
[26] F. Badway, A.N. Mansour, N. Pereira, J.F. Al-Sharab, F. Cosandey, I. Plitz, et al., Chem. Mater. 19 (2007) 4129.
[27] P. Poizot, S. Laruelle, S. Grugeon, L. Dupont, J.M. Tarascon, Nature 407 (2000) 496.
[28] A. Débart, L. Dupont, P. Poizot, J.-B. Leriche, J.M. Tarascon, J. Electrochem. Soc. 148 (2001) A1266.
[29] S. Grugeon, S. Laruelle, L. Dupont, J.M. Tarascon, Solid State Sci. 5 (2003) 895.
[30] T. Ohzuku, Z. Takehara, S. Yoshizawa, Electrochim. Acta 24 (1979) 219.
[31] L. Kavan, D. Fattakhova, P. Krtil, J. Electrochem. Soc. 146 (1999) 1375.
[32] C. Jiang, I. Honma, T. Kudo, H. Zhou, Electrochem. Solid-State Lett. 10 (2007) A127.
[33] F. Jiao, P.G. Bruce, Adv. Mater. 19 (2007) 657.
[34] C.K. Chan, H. Peng, G. Liu, K. McIlwrath, X.F. Zhang, R.A. Huggins, et al., Nat. Nano 3 (2008) 31.
[35] C. Delmas, H. Cognacauradou, J.M. Cocciantelli, M. Menetrier, J.P. Doumerc, Solid State Ionics 69 (1994) 257.
[36] M.W.W.J.H. Borghols, U. Lafont, E.M. Kelder, F.M. Mulder, J. Am. Chem. Soc. 131 (2009) 17786.
[37] Y. Liu, M. Clark, Q. Zhang, D. Yu, D. Liu, J. Liu, et al., Adv. Energy Mater. 1 (2011) 194.
[38] Y.Y. Liu, J.G. Li, Q.F. Zhang, N. Zhou, E. Uchaker, G.Z. Cao, Electrochem. Commun. 13 (2011) 1276.
[39] N. Meethong, H.-Y.S. Huang, W.C. Carter, Y.-M. Chiang, Electrochem. Solid State Lett. 10 (2007) A134.
[40] G. Kobayashi, S.-I. Nishimura, M.-S. Park, R. Kanno, M. Yashima, T. Ida, et al., Adv. Funct. Mater. 19 (2009) 395.
[41] M. Wagemaker, D.P. Singh, W.J. Borghols, U. Lafont, L. Haverkate, V.K. Peterson, et al., J. Am. Chem. Soc. 133 (2011) 10222.
[42] A.G. Dylla, G. Henkelman, K.J. Stevenson, Acc. Chem. Res. 46 (2013) 1104.
[43] M. Zukalova, M. Kalbac, L. Kavan, I. Exnar, M. Graetzel, Chem. Mater. 17 (2005) 1248.
[44] Y.-M. Jiang, K.-X. Wang, H.-J. Zhang, J.-F. Wang, J.-S. Chen, Sci. Rep. 3 (2013).
[45] K. Zhu, Q. Wang, J.-H. Kim, A.A. Pesaran, A.J. Frank, J. Phys. Chem. C 116 (2012) 11895.
[46] M. Wagemaker, F.M. Mulder, A. Van der Ven, Adv. Mater. 21 (2009) 2703.
[47] W.J.H. Borghols, M. Wagemaker, U. Lafont, E.M. Kelder, F.M. Mulder, J. Am. Chem. Soc. 131 (2009) 17786.
[48] S.-K. Jung, H. Gwon, J. Hong, K.-Y. Park, D.-H. Seo, H. Kim, et al., Adv. Energy Mater. 4 (2014).
[49] F. Lin, I.M. Markus, D. Nordlund, T.-C. Weng, M.D. Asta, H.L. Xin, et al., Nat. Commun. 5 (2014).
[50] M. Wagemaker, W.J.H. Borghols, F.M. Mulder, J. Am. Chem. Soc. 129 (2007) 4323.
[51] B.V. Ratnakumar, M.C. Smart, S. Surampudi, J. Power Sources 97—98 (2001) 137.
[52] F. Béguin, F. Chevallier, C. Vix-Guterl, S. Saadallah, V. Bertagna, J.N. Rouzaud, et al., Carbon 43 (2005) 2160.
[53] M. Jo, Y.-S. Hong, J. Choo, J. Cho, J. Electrochem. Soc. 156 (2009) A430.
[54] J.L. Lei, L.J. Li, R. Kostecki, R. Muller, F. McLarnon, J. Electrochem. Soc. 152 (2005) A774.
[55] N.P.W. Pieczonka, Z. Liu, P. Lu, K.L. Olson, J. Moote, B.R. Powell, et al., J. Phys. Chem. C 117 (2013) 15947.
[56] D.H. Jang, Y.J. Shin, S.M. Oh, J. Electrochem. Soc. 143 (1996) 2204.
[57] D.H. Jang, S.M. Oh, J. Electrochem. Soc. 144 (1997) 3342.
[58] E. Markevich, G. Salitra, D. Aurbach, Electrochem. Commun. 7 (2005) 1298.
[59] N. Kumagai, S. Komaba, Y. Kataoka, M. Koyanagi, Chem. Lett. 29 (2000) 1154.
[60] T.-F. Yi, Y.-R. Zhu, X.-D. Zhu, J. Shu, C.-B. Yue, A.-N. Zhou, Ionics 15 (2009) 779.
[61] N. Balke, S. Jesse, A.N. Morozovska, E. Eliseev, D.W. Chung, Y. Kim, et al., Nat. Nano 5 (2010) 749.
[62] M.N. Ou, S.R. Harutyunyan, S.J. Lai, C.D. Chen, T.J. Yang, Y.Y. Chen, Phys. Status Solidi (B) 244 (2007) 4512.
[63] G. Cao, Y. Wang, Characterization and Properties of Nanomaterials, 2nd ed., World Scientific Publishing Co. Pte. Ltd., 5 Toh Tuck Link, Singapore 596224, 2011.
[64] M. Ebner, D.-W. Chung, R.E. Garcia, V. Wood, Adv. Energy Mater. (2013).
[65] B. Vijayaraghavan, D.R. Ely, Y.-M. Chiang, R. García-García, R.E. García, J. Electrochem. Soc. 159 (2012) A548.
[66] J.S. Newman, C.W. Tobias, J. Electrochem. Soc. 109 (1962) 1183.

[67] M. Ebner, F. Geldmacher, F. Marone, M. Stampanoni, V. Wood, Adv. Energy Mater. 3 (2013) 845.
[68] T.R. Ferguson, M.Z. Bazant, J. Electrochem. Soc. 159 (2012) A1967.
[69] J. Newman, W. Tiedemann, AlChE J. 21 (1975) 25.
[70] W. Tiedemann, J. Newman, J. Electrochem. Soc. 122 (1975) 1482.
[71] J.F. Martin, A. Yamada, G. Kobayashi, S. Nishimura, R. Kanno, D. Guyomard, et al., Electrochem. Solid-State Lett. 11 (2008) A12.
[72] H. Li, L.H. Shi, Q. Wang, L.Q. Chen, X.J. Huang, Solid State Ionics 148 (2002) 247.
[73] S.K. Martha, E. Markevich, V. Burgel, G. Salitra, E. Zinigrad, B. Markovsky, et al., J. Power Sources 189 (2009) 288.
[74] D. Aurbach, B. Markovsky, A. Rodkin, M. Cojocaru, E. Levi, H.-J. Kim, Electrochim. Acta 47 (2002) 1899.
[75] J.S. Sakamoto, B. Dunn, J. Electrochem. Soc. 149 (2002) A26.
[76] D. Bresser, E. Paillard, M. Copley, P. Bishop, M. Winter, S. Passerini, J. Power Sources 219 (2012) 217.
[77] J. Syzdek, M. Marcinek, R. Kostecki, J. Power Sources 245 (2014) 739.
[78] J. Liu, G. Cao, Z. Yang, D. Wang, D. Dubois, X. Zhou, et al., ChemSusChem 1 (2008) 676.
[79] Y.-X. Yin, S. Xin, Y.-G. Guo, Part. Part. Syst. Charact. 30 (2013) 737.
[80] L. Zhou, P. O'Brien, J. Phys. Chem. Lett. 3 (2012) 620.
[81] F.C. Meldrum, H. Coelfen, Nanoscale 2 (2010) 2326.
[82] Y. Wang, G.Z. Cao, Chem. Mater. 18 (2006) 2787.
[83] Y. Oaki, H. Imai, Nanoscience: Vol. 1: Nanostructures through Chemistry, The Royal Society of Chemistry, 2013, pp. 1.
[84] R.-Q. Song, H. Coelfen, CrystEngComm 13 (2011) 1249.
[85] V.M. Yuwono, N.D. Burrows, J.A. Soltis, R.L. Penn, J. Am. Chem. Soc. 132 (2010) 2163.
[86] H.G. Yang, C.H. Sun, S.Z. Qiao, J. Zou, G. Liu, S.C. Smith, et al., Nature 453 (2008) 638.
[87] B. Wu, C. Guo, N. Zheng, Z. Xie, G.D. Stucky, J. Am. Chem. Soc. 130 (2008) 17563.
[88] X. Li, C. Ni, F. Chen, X. Lu, Z. Chen, J. Solid State Chem. 182 (2009) 2185.
[89] J. Ma, J. Teo, L. Mei, Z. Zhong, Q. Li, T. Wang, et al., J. Mater. Chem. 22 (2012) 11694.
[90] A.G. Dylla, P. Xiao, G. Henkelman, K.J. Stevenson, J. Phys. Chem. Lett. 3 (2012) 2015.
[91] W.Q. Fang, X.-Q. Gong, H.G. Yang, J. Phys. Chem. Lett. 2 (2011) 725.
[92] R.L. Penn, J.A. Soltis, CrystEngComm 16 (2014) 1409.
[93] R.L. Penn, J. Phys. Chem. B 108 (2004) 12707.
[94] N. Zheng, X. Bu, P. Feng, Nature 426 (2003) 428.
[95] S. Boris, B. Josip, Theoretical, Handbook of Zeolite Science and Technology, CRC Press, 2003.
[96] C.R.A. Catlow, S.C. David, W.L. Dewi, J.C.G. Pereira, S. Ben, Handbook of Zeolite Science and Technology, CRC Press, 2003.
[97] J.S. Chen, Y.L. Tan, C.M. Li, Y.L. Cheah, D. Luan, S. Madhavi, et al., J. Am. Chem. Soc. 132 (2010) 6124.
[98] Z. Yang, D. Choi, S. Kerisit, K.M. Rosso, D. Wang, J. Zhang, et al., J. Power Sources 192 (2009) 588.
[99] Y. Ren, L.J. Hardwick, P.G. Bruce, Angew. Chem. Int. Ed. 49 (2010) 2570.
[100] L. Zhou, D.S. Boyle, P. O'Brien, Chem. Commun. (2007) 144.
[101] L. Zhou, D. Smyth-Boyle, P. O'Brien, J. Am. Chem. Soc. 130 (2008) 1309.
[102] D. Zhang, G. Li, F. Wang, J.C. Yu, CrystEngComm 12 (2010) 1759.
[103] S.-J. Liu, J.-Y. Gong, B. Hu, S.-H. Yu, Cryst. Growth Des. 9 (2009) 203.
[104] Z. Hong, M. Wei, T. Lan, L. Jiang, G. Cao, Energy Environ. Sci. 5 (2012) 5408.
[105] Z. Hong, M. Wei, T. Lan, G. Cao, Nano Energy 1 (2012) 466.
[106] J. Ye, W. Liu, J. Cai, S. Chen, X. Zhao, H. Zhou, et al., J. Am. Chem. Soc. 133 (2011) 933.
[107] Z. Hong, Y. Xu, Y. Liu, M. Wei, Chemistry 18 (2012) 10753.
[108] Y.Q. Zheng, E.R. Shi, Z.Z. Chen, W.J. Li, X.F. Hu, J. Mater. Chem. 11 (2001) 1547.
[109] J. Ning, T. Jiang, K. Men, Q. Dai, D. Li, Y. Wei, et al., J. Phys. Chem. C 113 (2009) 14140.
[110] S. Chen, M. Wang, J. Ye, J. Cai, Y. Ma, H. Zhou, et al., Nano Res. 6 (2013) 243.
[111] Y.-D. Ko, J.-G. Kang, J.-G. Park, S. Lee, D.-W. Kim, Nanotechnology 20 (2009) 455701.
[112] J. Wang, N. Du, H. Zhang, J. Yu, D. Yang, J. Phys. Chem. C 115 (2011) 11302.
[113] M. Xu, F. Wang, B. Ding, X. Song, J. Fang, RSC Adv. 2 (2012) 2240.
[114] Z. An, J. Zhang, S. Pan, F. Yu, J. Phys. Chem. C 113 (2009) 8092.
[115] X. Duan, L. Mei, J. Ma, Q. Li, T. Wang, W. Zheng, Chem. Commun. 48 (2012) 12204.
[116] E. Uchaker, M. Gu, N. Zhou, Y. Li, C. Wang, G. Cao, Small 9 (2013) 3880.
[117] J.F. Liu, Q.H. Li, T.H. Wang, D.P. Yu, Y.D. Li, Angew. Chem. Int. Ed. 43 (2004) 5048.
[118] G. Li, K. Chao, H. Peng, K. Chen, Z. Zhang, Inorg. Chem. 46 (2007) 5787.
[119] G. Li, K. Chao, C. Zhang, Q. Zhang, H. Peng, K. Chen, Inorg. Chem. 48 (2009) 1168.
[120] C. Lausser, H. Coelfen, M. Antonietti, ACS Nano 5 (2011) 107.
[121] Y. Liu, E. Uchaker, N. Zhou, J. Li, Q. Zhang, G. Cao, J. Mater. Chem. 22 (2012) 24439.
[122] C.H. Sun, X.H. Yang, J.S. Chen, Z. Li, X.W. Lou, C. Li, et al., Chem. Commun. 46 (2010) 6129.
[123] A.M. Cao, J.S. Hu, H.P. Liang, L.J. Wan, Angew. Chem. Int. Ed. 44 (2005) 4391.
[124] J. Liu, D. Xue, Nanoscale Res. Lett. 5 (2010) 1525.
[125] F. Dang, T. Hoshino, Y. Oaki, E. Hosono, H. Zhou, H. Imai, Nanoscale 5 (2013) 2352.
[126] A. Cao, A. Manthiram, Phys. Chem. Chem. Phys. 14 (2012) 6724.
[127] N. Zhou, Y. Liu, J. Li, E. Uchaker, S. Liu, K. Huang, et al., J. Power Sources 213 (2012) 100.
[128] I. Bilecka, A. Hintennach, I. Djerdj, P. Novak, M. Niederberger, J. Mater. Chem. 19 (2009) 5125.
[129] Y. Xia, W.K. Zhang, H. Huang, Y.P. Gan, J. Tian, X.Y. Tao, J. Power Sources 196 (2011) 5651.
[130] M. Chen, F. Teng, G. Li, H. Shi, J. Wang, M. Xu, et al., Ionics 18 (2012) 541.
[131] H. Yang, X.-L. Wu, M.-H. Cao, Y.-G. Guo, J. Phys. Chem. C 113 (2009) 3345.
[132] J. Popovic, R. Demir-Cakan, J. Tornow, M. Morcrette, D.S. Su, R. Schloegl, et al., Small 7 (2011) 1127.
[133] N. Zhou, H.-Y. Wang, E. Uchaker, M. Zhang, S.-Q. Liu, Y.-N. Liu, et al., J. Power Sources 239 (2013) 103.
[134] J. Fang, B. Ding, H. Gleiter, Chem. Soc. Rev. 40 (2011) 5347.
[135] K.X. Yao, H.C. Zeng, J. Phys. Chem. C 113 (2009) 1373.
[136] P. Tartaj, J.M. Amarilla, Adv. Mater. 23 (2011) 4904.
[137] P. Tartaj, Chem. Commun. 47 (2011) 256.
[138] A.-Y. Zhang, L.-L. Long, W.-W. Li, W.-K. Wang, H.-Q. Yu, Chem. Commun. 49 (2013) 6075.
[139] L. Zhou, J. Chen, C. Ji, L. Zhou, P. O'Brien, CrystEngComm 15 (2013) 5012.
[140] R.O. Da Silva, R.H. Goncalves, D.G. Stroppa, A.J. Ramirez, E.R. Leite, Nanoscale 3 (2011) 1910.
[141] Q. Chen, C. Chen, H. Ji, W. Ma, J. Zhao, RSC Adv. 3 (2013) 17559.
[142] Y. Liu, Y. Zhang, J. Wang, CrystEngComm 15 (2013) 791.

[143] J.-Y. Dong, W.-H. Lin, Y.-J. Hsu, D.S.-H. Wong, S.-Y. Lu, CrystEngComm 13 (2011) 6218.
[144] Z. Bian, T. Tachikawa, W. Kim, W. Choi, T. Majima, J. Phys. Chem. C 116 (2012) 25444.
[145] X. Yang, J. Qin, Y. Li, R. Zhang, H. Tang, J. Hazard. Mater. 261 (2013) 342.
[146] L. Zhang, X.-F. Cao, Y.-L. Ma, X.-T. Chen, Z.-L. Xue, New J. Chem. 34 (2010) 2027.
[147] Y. Yang, Y. Yang, H. Wu, S. Guo, CrystEngComm 15 (2013) 2608.
[148] S. Sun, X. Zhang, J. Zhang, L. Wang, X. Song, Z. Yang, CrystEngComm 15 (2013) 867.
[149] J. Sun, G. Chen, J. Pei, R. Jin, Q. Wang, X. Guang, J. Mater. Chem. 22 (2012) 5609.
[150] Q. Kuang, S. Yang, ACS Appl. Mater. Interfaces 5 (2013) 3683.
[151] S. Deng, V. Tjoa, H.M. Fan, H.R. Tan, D.C. Sayle, M. Olivo, et al., J. Am. Chem. Soc. 134 (2012) 4905.
[152] D. Wang, J. Sun, X. Cao, Y. Zhu, Q. Wang, G. Wang, et al., J. Mater. Chem. A 1 (2013) 8653.
[153] Y. Liu, G. Zhu, B. Ge, H. Zhou, A. Yuan, X. Shen, CrystEngComm 14 (2012) 6264.
[154] T. Ikeda, Y. Oaki, H. Imai, Chem. Asian. J. 8 (2013) 2064.
[155] X. Hu, J. Gong, L. Zhang, J.C. Yu, Adv. Mater. 20 (2008) 4845.
[156] B. Hu, L.-H. Wu, Z. Zhao, M. Zhang, S.-F. Chen, S.-J. Liu, et al., Nano Res. 3 (2010) 395.
[157] X.L. Wu, S.J. Xiong, Z. Liu, J. Chen, J.C. Shen, T.H. Li, et al., Nat. Nano 6 (2011) 103.
[158] G. Zhu, Y. Liu, C. Zhang, Z. Zhu, Z. Xu, Chem. Lett. 39 (2010) 994.
[159] G. Donnay, D.L. Pawson, Science 166 (1969) 1147.
[160] M.E. Marsh, Biomineralization, Wiley-VCH Verlag GmbH & Co. KGaA, 2005, pp. 195.
[161] J. Ge, Y. Hu, M. Biasini, W.P. Beyermann, Y. Yin, Angew. Chem. Int. Ed. 46 (2007) 4342.
[162] T. Lee, C. Zhang, Pharm. Res. 25 (2008) 1563.
[163] M. Kijima, Y. Oaki, H. Imai, Chem. Eur. J. 17 (2011) 2828.

Evan Uchaker received his BS from The Ohio State University in 2010, and is currently a PhD student under the supervision of Professor Guozhong Cao in the Department of Materials Science and Engineering at the University of Washington. His research interests are focused on the synthesis and characterization of nanostructured architectures and disordered electrode materials for electrochemical energy storage devices such as alkali-ion and redox flow batteries.

Guozhong Cao is Boeing-Steiner Professor of Materials Science and Engineering, Professor of Chemical Engineering, and Adjunct Professor of Mechanical Engineering at University of Washington, and also a Professor at Beijing Institute of Nanoenergy and Nanosystems, Chinese Academy of Sciences and Dalian University of Technology. His current research is focused on chemical processing of nanomaterials for energy related applications including solar cells, rechargeable batteries, supercapacitors, and hydrogen storage.